2009

Determination of nanogram mass and measurement of polymer solution free volume using thickness-shear mode (tsm) quartz resonators

Anthony James Richardson
University of South Florida

Determination of Nanogram Mass and Measurement of Polymer Solution Free Volume Using Thickness-Shear Mode (TSM) Quartz Resonators

by

Anthony James Richardson

A thesis submitted in partial fulfillment
of the requirements for the degree of
Master of Science in Chemical Engineering
Department of Chemical and Biomedical Engineering
College of Engineering
University of South Florida

Major Professor: Venkat R. Bhethanabotla, Ph.D.
Scott W. Campbell, Ph.D.
Ryan Toomey, Ph.D.
Thomas M. Weller, Ph.D.

Date of Approval
October 16, 2009

Keywords: Free volume, mass sensitivity, nanobalance, shear modulus, TSM quartz resonator

DEDICATION

This thesis is dedicated to my parents, Douglas and Jill, and my brother, Jason Richardson.

ACKNOWLEDGEMENTS

I would like to express gratitude to Dr. Venkat R. Bhethanabotla for his support and guidance as my major advisor in my research endeavors both as an undergraduate and graduate student. Also, I would like to thank Allan Smith (Masscal), Stefan Cular (DTRA), Subramanian Sankaranarayanan (Harvard), and Reetu Singh (USF) for their technical help and contributions in programming of analytical models in this work. Assistance from John Furry (Masscal) with the Masscal G1 apparatus is acknowledged.

TABLE OF CONTENTS

LIST OF TABLES

LIST OF FIGURES

Determination of Nanogram Mass and Measurement of Polymer Solution Free Volume Using Thickness-Shear Mode (TSM) Quartz Resonators

Anthony James Richardson

ABSTRACT

More commonly referred to as a quartz crystal microbalance (QCM), thickness-shear mode (TSM) quartz resonator devices utilize an acoustic wave to establish a bulk-detection mechanism prompting their utilization as gravimetric sensors with nanogram mass sensitivity and capability to measure various film property dynamics, due to variations in the system environment, of thin-films that are uniformly distributed across the resonator surface. The development of an absolute TSM-based nanobalance and an experimental technique using conventional TSM resonators for the real-time measurement of the change in the viscoelastic shear modulus and fractional free-hole volume of a poly(isobutylene) film due to the sorption of various organic vapors are presented in this thesis work.

Development of an electrode-modified TSM quartz resonator that is responsive to nanogram mass loadings, while exhibiting a mass sensitivity profile that is independent of material placement on the sensor platform, is detailed in this thesis work. The resulting nanogram balance would greatly enhance the field of mass measurement and become useful in applications such as droplet gravimetry, the study of non-volatile residue (NVR) contamination in solvents. A ring electrode design predicted by an

analytical theory for sensitivity distribution to achieve the desired uniform mass sensitivity distribution is presented in this work. Using a microvalve capable of depositing nanogram droplets of a polymer solution, and a linear stepping stage for radial positioning of these droplets across the sensor platform, measurements of the mass sensitivity distributions were conducted and are presented. The measurements agree well with theory. Further improvements are possible and are identified to achieve better uniformity and to reduce the instability in the resonant frequency of these devices. Additionally, droplet gravimetric results for NVR in methanol droplets using the modified TSM devices are presented, which compare well with determinations made by evaporation of larger volumes of the stock solutions.

Storage modulus, G', loss modulus, G'', and, consequently, the shear modulus, G ($G = G' + jG''$), of polymer and polymer/solvent systems were measured in this work using a TSM quartz resonator. The polymer poly(isobutylene) was spin-coated as a film of a few microns thickness on the surface of the TSM device and, upon inducing oscillation of the device at its resonance frequency (several mega-Hertz), the impedance characteristics were measured. In addition, the poly(isobutylene) film was exposed to known weight concentrations, up to 20%, of benzene, chloroform, n-hexane, and dichloromethane vapors diluted in nitrogen gas, and the impedance characteristics were measured. Data collected from the impedance analyzer were examined by modeling the polymer and polymer/solvent loaded TSM device with an electrical equivalent circuit and a mechanical perturbation model to reliably yield the shear modulus. Using a superposition theory and the shear modulus, the fractional free volume of the polymer/solvent systems were determined. These results correlate well with values found using the Vrentas-Duda free-volume (FV) theory. A novel experimental technique for measuring fractional free-hole volumes of polymer/solvent mixtures is established in this thesis work.

CHAPTER 1

INTRODUCTION

1.1 Motivation

The motivation for measuring the viscoelastic shear moduli and the fractional free-hole volume of polymer/solvent systems, as well as, the development of a TSM-based nanobalance are described below.

Given the importance of polymer films in industrial applications and the lack of polymer property data in literature, it is useful to study polymers and their dynamics within environments whose conditions are subject to change. Characterizing the diffusive transfer of sorbents within a polymer film and the effects the sorbent have on the film are important in scientific and industrial research. To accurately describe the diffusion of a species through a polymer film and extract a diffusion coefficient, it is necessary to determine the free-hole volume of the polymer system which is the predominant driving force for diffusive mass transfer through a rubbery polymer film. A technique utilizing a TSM resonator for the real-time determination of the polymer free-volume through monitoring the changes in the viscoelasticity of pure polymer and sorbent-loaded polymer films is established in this work. A study of the viscoelastic shear moduli upon the sorption of varying concentrations of benzene, chloroform, n-hexane, and dichloromethane vapors in a poly(isobutylene) film using a TSM resonator was performed in this thesis work. From the shear moduli data and a superposition

principle, the fractional free-hole volume of poly(isobutylene)/solvent systems was extracted.

Utilizing available TSM resonators for gravimetric analysis down to the nanogram level is possible provided that the deposited mass is uniformly distributed and coupled across the active area of the device surface. A uniform film is necessary because the mass sensitivity is non-uniform decreasing across the resonator surface in a Gaussian-like distribution extending from the center to the edge of the substrate. The non-uniformity in mass sensitivity precludes the use of current TSM devices as absolute mass balances. Modification of the electrode geometry, the influencing factor setting the mass sensitivity profile, was conducted in this thesis work to establish an active area exhibiting uniform mass sensitivity in order to create an absolute TSM-based nanobalance. A working TSM-based nanobalance would allow the mass measurement of any nano-scale mass loading deposited within the area of constant mass sensitivity including non-uniform films such as non-volatile residue (NVR) from an evaporated solvent droplet. Additionally, the reliance on mechanical/analytical mass balances, which are expensive, limited to microgram mass sensitivity, and susceptible to mechanical vibration instability, can be reduced with the advent of a TSM nanobalance.

1.2 Thickness-Shear Mode (TSM) Quartz Resonators

Typically referred to as a quartz crystal microbalance (QCM), a TSM quartz resonator consists of a quartz disk, the thickness of which depends upon the operating resonance frequency, with metallic planar electrodes deposited on both faces. Placement of a constant voltage load between the parallel electrodes results in the formation of an electric field. The applied electric field prompts mechanical vibration of the quartz substrate due to the piezoelectric effect. Initially, the amplitude of vibration is small, however, when the frequency of the driving field approaches the natural harmonics of the quartz substrate, resonance in the quartz is observed. Typical resonance frequencies are between 5 and 10 MHz [1, 2]. Resonance initiates the propagation of a shear horizontal

wave through the substrate establishing the bulk-detection mechanism of TSM resonators.

1.3 Applications of TSM Resonators

Due to their inherent bulk-detection mechanism resulting from the shear-horizontal wave perturbation of the piezoelectric substrate, TSM resonators are utilized in a multitude of industrial and scientific applications. TSM resonators have recently been employed as reliable sensors for thin-film properties, contaminants in liquid and gaseous environments using a thin selective/sensitive film deposited across the device surface, characterizing the sorption/desorption of a species in a sorbent material, studies of biological and chemical reaction kinetics, corrosion monitoring, detection of biomarkers in biological environments, *et cetera*. However, the primary industrial application of these devices is as thickness monitors in deposition processes such as chemical vapor deposition (CVD) of thin metallic films. Based on the frequency shift of the resonator, the thickness of a uniformly developing film can be monitored in real-time.

1.4 Thesis Organization

Divided into six chapters, the following thesis work details two major projects conducted pertaining to TSM resonators. Chapter 1 presents a fundamental discussion of TSM resonators and their widespread applications. A discussion of the extraction of the viscoelastic shear modulus and fractional free-hole volume of polymer/solvent systems using TSM resonators including polymer/solvent solution thermodynamics, a combined equivalent circuit/mechanical perturbation model, a superposition principle, and a theoretical FV model are presented in Chapter 2. Chapter 3 presents the design and development of a TSM-based nanobalance for absolute gravimetry of mass loadings down to the nanogram level. Experimental and data-extraction details for the measurement of the viscoelastic shear-moduli of polymer/solvent systems and the

fabrication and testing of electrode-modified TSM resonators are given in Chapter 4. Chapter 5 presents the results and detailed discussions of these results for the TSM resonator applications discussed in Chapters 2 and 3. Conclusions and suggestions for future work are given in Chapter 6.

CHAPTER 2

VISCOELASTIC SHEAR MODULUS AND FRACTIONAL FREE-HOLE VOLUME OF POLYMER/SOLVENT SYSTEMS

2.1 Introduction

To viably utilize a polymer as a diffusive membrane, sensitive/selective sensing film, catalyst or catalytic platform, drug encapsulate, *et cetera*, it is essential to characterize the properties and dynamics of a thin-polymer film within these application environments. Fortunately, development of analytical/simulation and experimental techniques to characterize changes in polymer film properties resulting from variations in system environments including temperature, pressure, or the addition of sorbents has been extensive over the past few decades. Typically, polymer films are employed as thin-films (< 1 micron) or small-mass depositions (a few nanograms) making it difficult to evaluate their macroscopic/microscopic properties using conventional microscopy, spectroscopic, chromatographic, or fluorometric techniques. However, due to their nanogram mass sensitivity, TSM resonators are used prevalently to accurately measure and characterize polymer thin-film properties. Given the mechanical detection mechanism of bulk-acoustic wave devices, measurements of bulk-film property dynamics of pure polymer and solvent-loaded polymer films deposited on the surface of any piezoelectric-substrate TSM device are possible. Recent film property studies using TSM resonators have focused extensively on viscosity, phase changes (i.e. film-state transitions), thermodynamic properties, and diffusion rates due to changes in temperature or upon the sorption of analytes. In this thesis work, characterization of the viscoelastic

shear modulus and, subsequently, the fractional free-hole volume of polymer/solvent systems using a TSM resonator were conducted.

2.1.1 Viscoelastic Shear Moduli of Polymer Films

Wave propagation into the bulk of a viscoelastic film coupled to the surface of a TSM resonator can result in significant dynamic film behavior. At the film/resonator interface, the viscoelastic film is driven synchronously with the resonator surface, however, in the upper regions of the film, substantial acoustic phase shift or lagging is observed resulting in an increase in shear deformation across the film thickness. Figure 2.1 illustrates the shear deformation in a viscoelastic film that is perturbated by a shear horizontal wave. The establishment of a shear deformation gradient across the film causes elastic energy to be stored and dissipated in the film. A physical property that quantifies the effects of an applied shear stress and energy dynamics in a viscoelastic film is the complex shear modulus, G, which accounts for elastic energy density, represented by a storage modulus, G', and power dissipation, loss modulus, G". The overall expression for the complex shear modulus is $G = G' + jG"$ [3]. Depending on the type of viscoelastic film and system conditions (i.e. pressure, temperature, or presence of an adsorbed species), the shear modulus can vary significantly. For pure polymer films, the magnitude of G is on the order of 10^{10} dyne/cm^2 for a film in its glassy state (low temperature) and 10^7 dyne/cm^2 for the rubbery state (moderate/high temperature) [4]. The polymer poly(isobutylene) used in this study is tested at standard conditions and remains in its rubbery state regardless of solvent sorption.

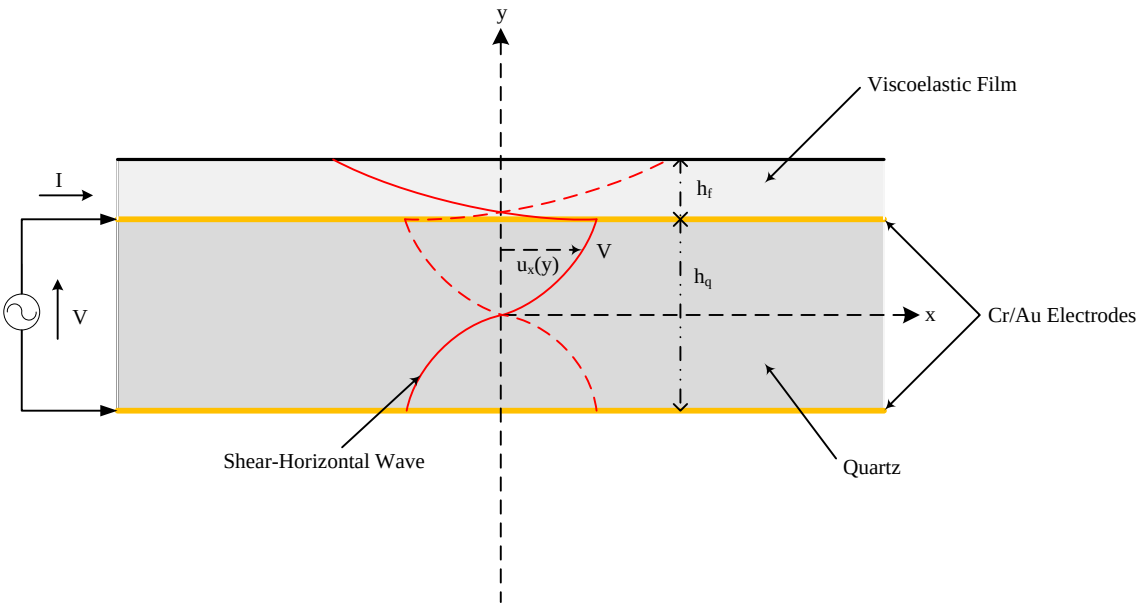

Figure 2.1: A cross-sectional view of the shear-horizontal wave propagation through the quartz substrate and a viscoelastic layer coupled to the device surface.

2.1.2 Fractional Free-Hole Volume of Polymer Films

A significant property influencing diffusion of gas molecules through a compliant film was introduced by Cohen and Turnbull in the 1950s which is the concept of "free-hole" volume [5]. The free volume is defined as the volume not occupied by adjacent molecules in a fluid system. Given the rigid and compact nature of the molecular framework of a polymer film, the mass transfer or self-diffusion of a penetrant species becomes dependent on the available volume between inter-locked monomer chains. Additionally, the energy of the penetrant to overcome attractive forces that inhibit migration between voids or holes in the chains is important. For diffusion of low-molecular weight species in a polymer film, thermodynamic fluctuations in the film, without significant change in system energy, cause a random redistribution of free volume which increases the probability of species migration [6, 7], thereby, establishing the free-hole volume as the driving force for molecular transfer. These fluctuations for polymer/solvent systems are described well by the thermodynamic model in Section 2.3.2. Some methods, analytical (i.e. equations of state) and experimental (e.g. positron

annihilation spectroscopy [8]), have been developed to quantify the free volume of polymer systems. In this thesis work, a technique is proposed for determining the fractional free-hole volume of a solvent-loaded polymer film, the ratio of the available free volume to the total volume of the polymer system, using a TSM resonator.

2.2 Sorption of Organic Solutes in Polymer Films

A great deal of confusion as to what constitutes sorption mass transfer of a solute in a solid or liquid exists. Defining this concept accurately is important for the understanding of solvent activity in a polymer film as the changes in film properties are sensitive to the extent of penetration of the solute. In this work, the system regimes that were studied involved intimate mixtures formed through absorption of the solvent in to the polymer film. These solutions are equivalent to mixtures of small molecules that are in complete miscible form such as ethanol and water.

2.3 Polymer/Solvent Mixture Thermodynamics

To reliably extract the viscoelastic shear modulus of a solvent-loaded polymer film requires the characterization of the extent of sorption of a solvent into the polymer film. Sorption of the solvent will alter the morphology of the polymer and consequently the film thickness and mixture density. The extent of sorption is measured by the weight fraction of the solvent in the polymer. Typically, the weight fraction can be measured directly using a TSM resonator coated with a sensitive/selective polymer film as a mass balance. As long as the pure polymer and solvent-loaded polymer film can be treated as an ideal mass layer, the individual mass loadings associated with the polymer film and the absorbed solvent can be determined by the resonator using the modified Sauerbrey model, which is described in section 2.4.1. However, in this thesis work, the polymer and solvent-loaded polymer films are of thicknesses in the viscoelastic regime and do not exhibit ideal mass behavior. Measuring the viscoelastic properties of these films using

the TSM resonator precludes the direct mass determination because dampening of the mechanical/electrical properties of the resonator is attributed to both the mass loading and viscoelastic effects caused by wave propagation in the bulk film [9]. Consequently, reliable polymer/solvent solution thermodynamics must be considered to determine the weight fraction of the solvent in the polymer film.

2.3.1 Vapor/Liquid Equilibrium Modeling

Before the activity of the solvent in the polymer film can be evaluated, the vapor/liquid equilibrium (VLE) between the generated solvent vapor and the inert carrier gas, nitrogen, must be established. This is achieved by equating the vapor and liquid fagacities of the solvent in solution. The following equilibrium model, Equations (2-1) through (2-11), was derived by Upadhyayula *et al* (see Equations (2-1) through (2-14) in Ref. [10]).

$$f_1^{liquid} = f_1^{vapor} \tag{2.1}$$

Where, f_1^{liquid} and f_1^{vapor} are the liquid and vapor fagacities of the solvent, respectively. By definition, the fagacities of the solvent in the liquid and vapor phases are as followed:

$$y_1 P \widehat{\Phi}_1^v = \gamma_1 x_1 f_1^l \tag{2.2}$$

For a binary mixture, the fugacity coefficient of the solvent in the vapor phase is:

$$\widehat{\Phi}_1^v = exp\left[\frac{P}{RT}\left(B_{11} + y_3^2(2B_{13} - B_{11} - B_{33})\right)\right] \tag{2.3}$$

Where, B_{11}, B_{13}, and B_{33} are second virial coefficients. The primary subscripts 1 and 3 denote the solvent and nitrogen gas, respectively. R is the ideal gas constant, P is the total system pressure, and T is the absolute system temperature. The second virial coefficient of the solvent, B_{11}, at the system temperature is estimated using a corresponding states theory developed by Tsonopoulos [11].

$$B_{11} = \frac{RT_c}{P_c}\left[f^{(0)}(T_R) + \omega f^{(1)}(T_R)\right] \tag{2.4}$$

Where, T_c and P_c are the critical temperature and pressure of the solvent. Pitzer's acentric or compressibility factor, ω, accounts for non-ideality of the component in the gas phase [12]. T_R and P_R are the reduced temperature and pressure of the solvent. The terms $f^{(0)}(T_R)$ and $f^{(1)}(T_R)$ are defined as [11]:

$$f^{(0)}(T_R) = 0.1445 - \frac{0.330}{T_R} - \frac{0.1358}{{T_R}^2} - \frac{0.0121}{{T_R}^3} \tag{2.5}$$

$$f^{(1)}(T_R) = 0.073 + \frac{0.46}{T_R} - \frac{0.50}{{T_R}^2} - \frac{0.097}{{T_R}^3} - \frac{0.0073}{{T_R}^8} \tag{2.6}$$

Calculated values of B_{11} and B_{13} for each solvent considered in this thesis at 298.15 K are tabulated in Table 2.1. The second virial coefficient of pure nitrogen gas, B_{33}, is -5.4 cm^3/mol.

Table 2.1: Second virial coefficients of the solvents at 298.15 K

Solvent	B_{11} (cm^3/mol)	B_{13} (cm^3/mol)
Benzene	-1758.7	-152
Chloroform	-2053.0	-134
n-Hexane	-1841.0	-168
Dichloromethane	-1315.5	-114

In the liquid phase, the solvent fugacity term, f_1^l, is given by the following expression.

$$f_1^l = P_1^{sat}\phi_1^{sat} exp\left[\frac{V_1^{sat}}{RT}(P - P_1^{sat})\right] \tag{2.7}$$

Where,

$$\phi_1^{sat} = exp\left[\frac{B_{11}P_1^{sat}}{RT}\right] \tag{2.8}$$

Here, P_1^{sat} is the saturation pressure of the pure solvent at the absolute system temperature, T. The exponential term in Equation (2.7) is known as the Poynting correction factor and, under mild pressure conditions, approaches unity. Many models are available for estimating the saturation pressure of volatile components including the well known Antoine equation, however, for best accuracy, Wagner's equation is utilized in this thesis work. The pressures are given in Torr.

$$ln\left(\frac{P_1^{sat}}{P_c}\right) = \frac{V_{PA}x + V_{PB}x^{1.5} + V_{PC}x^3 + V_{PD}x^6}{1 - x} \tag{2.9}$$

Let,

$$x = 1 - T_R$$

Saturation volume, V_1^{sat}, of the solvent at the system temperature, T, is correlated well with the modified Rackett equation.

$$V_1^{sat} = \frac{RT_c}{P_c} Z_{RA}^{[1+x^{2/7}]} \tag{2.10}$$

The Wagner equation constants [13] and the Rackett compressibility factor, Z_{RA}, [12] for each solvent considered in this thesis work are tabulated in Table 2.2.

Table 2.2: Wagner's equation constants and Rackett compressibility factors

Solvent	V_{PA}	V_{PB}	V_{PC}	V_{PD}	Z_{RA}
Benzene	-6.98270	1.33210	-2.6286	-3.3340	0.2698
Chloroform	-6.95546	1.16625	-2.1397	-3.4442	0.2750
n-Hexane	-7.46765	1.44211	-3.2822	-2.5094	0.2635
Dichloromethane	-7.35739	2.75460	-4.0704	3.5070	0.2618

After combining and simplifying the above equations, the general expression for the VLE model is:

$$\gamma_1 x_1 = a_1 = \frac{y_1 P exp\left[\frac{P}{RT}\left(B_{11} + y_3^2(2B_{13} - B_{11} - B_{33})\right)\right]}{P_1^{sat} exp\left[\frac{B_{11}P_1^{sat}}{RT}\right] exp\left[\frac{V_1^{sat}}{RT}(P - P_1^{sat})\right]} \quad (2.11)$$

Here, a_1 is the activity coefficient of the solvent. Equation (2.11) is based on the assumption that the fugacity of the solvent at the specified system conditions is equivalent to the fugacity at saturation [12].

2.3.2 Flory-Huggins Model for Polymer/Solvent Mixtures

The polymer/solvent solution thermodynamics is studied through the utilization of a modified Flory-Huggins model for the solvent activity in a polymer film. This model was presented by Upadhyayula *et al* (see Equations (2-15) through (2-22) in Ref. [10]) and is described below. The generalized Flory-Huggins model is given by the following expression [14-16].

$$ln(a_1) = ln(\Phi_1) + (1 - r)\Phi_2 + \chi{\Phi_2}^2 \quad (2.12)$$

Here,

$$r = \frac{V_1}{V_2}$$

$$\Phi_i = \frac{{}^{V_i}/_{M_i} w_i}{\sum_i {}^{V_i}/_{M_i} w_i} \tag{2.13}$$

Where, $\Phi_1$and Φ_2 are the solution volume fractions of the solvent and polymer, respectively. V_1 and V_2 are the molar specific volumes of the solvent and polymer. These are estimated through a summation of Van der Waals group volumes and are tabulated in Table 2.3 [17]. The group volume of poly(isobutylene) was determined from the mass-average molecular weight. Solvent and polymer weight fractions are expressed as w_1 and w_2, respectively.

Table 2.3: Molar specific volumes of each component at 298.15 K

Component	V_i $(cm^3 \cdot mol^{-1})$
Benzene	3.1878
Chloroform	2.870
n-Hexane	4.4998
Dichloromethane	3.2479
Poly(isobutylene)	20,184

The interaction parameter, χ, in Equation (2.12) accounts for the energy associated with the inter-dispersion of the solvent and polymer molecules [14]. Since the interaction parameter exhibits composition dependence, a linear regression model for χ based on experimental solvent activity data is utilized.

$$\chi = A\Phi_1 + B\Phi_2 \tag{2.14}$$

To derive the modified Flory-Huggins model, evaluation of the total Gibbs free energy of the polymer/solvent system is necessary. The total Gibbs free energy of the mixture assuming a linear dependence of χ with composition is [14, 15]:

$$\frac{nG^E}{RT} = n_1 \ln\left(\frac{\Phi_1}{x_1}\right) + n_2 \ln\left(\frac{\Phi_2}{x_2}\right) + \chi \Phi_1 \Phi_2 (n_1 + r n_2) \tag{2.15}$$

Here, A and B are regression coefficients. The number of total moles of solvent and polymer are given by n_1 and n_2, respectively. Taking the partial derivative of Equation 2.15 in terms of n_1 yields the expression for the solvent activity in the polymer film which is known as the modified Flory-Huggins model. It should be noted that the activity of the solvent in the polymer film is assumed to be equivalent to the activity in the vapor phase allowing the combination of Equations 2.11 and 2.16.

$$\ln(a_1) = \ln(1 - \Phi_1) + \left(1 - \frac{1}{r}\right)\Phi_2 + [2(A - B)\Phi_1 + B]{\Phi_2}^2 \tag{2.16}$$

Based on data from a previous gravimetric study of the sorption of organic vapors into an ideal-mass poly(isobutylene) film using a TSM resonator (described in Section 2.4.1), the Flory-Huggins regression parameters A and B were calculated using a non-linear Levenberg-Marquardt regression of Equation 2.16 (data from this internal study has not been published). The regression fits were compared to reliable free-volume (FV) models for predicting the molecular activity in mixtures including UNIFAC-FV [18] and Entropic-FV [19] and correlated well. The A and B parameters are tabulated in Table 2.4 for each poly(isobutylene)/solvent system considered in this work.

Table 2.4: Flory-Huggins regression parameters for each poly(isobutylene)/solvent system

Solvent	*A*	*B*
Benzene	0.6169	1.1618
Chloroform	0.3174	1.0627
n-Hexane	0.3471	0.8636
Dichloromethane	0.2540	1.5783

Given the good agreement between the experimental solvent activity data (*i.e.* the modified Flory-Huggins regression fit) and the FV models, the weight fractions of the solvent in the polymer for a film of a thickness within the viscoelastic regime can be extracted assuming the solvent activity is independent of film thickness.

2.4 Polymer/Solvent Mixture Film Properties

2.4.1 Film Thickness Determination

As mentioned previously, a primary industrial application of TSM resonators is the real-time thickness monitoring during thin-film deposition. Deposition of a foreign mass, either in the form of a thin mass layer or point mass that is inertially coupled to the device surface, causes a reduction in the resonance frequency. This reduction is due to the mechanical detection mechanism of bulk-acoustic wave sensors. In a bulk-acoustic wave device, the propagating wave is generated through the bulk of the piezoelectric substrate, in this case quartz. Since the wave propagates the entire substrate, it is expected that the wave would cross the surface boundary between the quartz and deposited mass. The transmission of the wave into the deposited mass alters the

characteristics of the wave propagation path, thereby, affecting the wave velocity or amplitude. The mechanical dampening of the wave by the added mass results in the reduced device frequency. Coupled mass loadings on the surface of a TSM resonator and their effects on the mechanical and electrical properties of the device have been well studied.

Provided that the mass loading is uniformly deposited across the resonator surface and of a thickness within the ideal mass regime, changes in the resonant frequency of the device can be directly correlated to the mass deposited and, subsequently, the film thickness. Several criteria must be followed to establish an ideal mass layer on the resonator surface. A mass exhibiting ideal behavior should be infinitesimally thick in comparison to the thickness of the quartz substrate. The electrode thickness is neglected. Additionally, the transverse oscillation of the film must remain in phase with the propagating wave meaning minimal shear deformation of the film must be observed. In other words, the shear displacement, $u_x(y)$, should be constant across the film thickness, h_f. [9, 20]. Figure 2.2 shows the motion of the shear-horizontal wave through the quartz substrate and an ideal mass layer coupled to the resonator surface. The mass layer moves synchronously with the quartz surface acting as merely an extenuation of the quartz substrate. To ensure ideal mass behavior, the added motional series circuit resistance of the resonator (described in Section 2.5.1) contributed from the total deposited mass should not exceed 100 ohms.

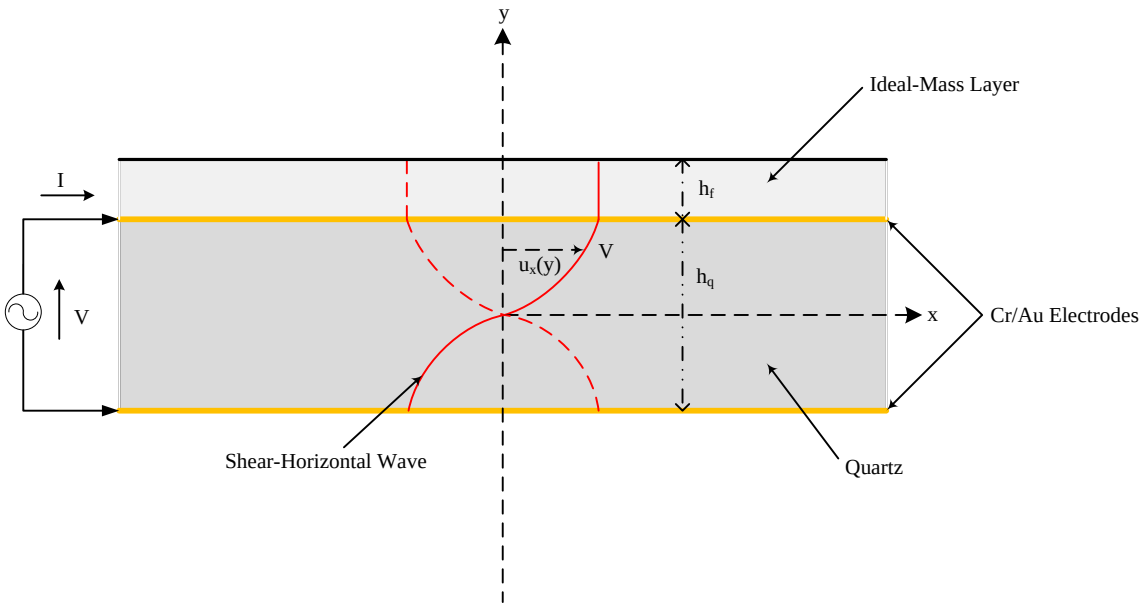

Figure 2.2: A cross-sectional view of the shear-horizontal wave propagation through the quartz substrate and an ideal-mass layer coupled to the device surface.

Developed by Sauerbrey in the early 1950s, a model for relating the frequency shift of the TSM resonator to the resultant mass loading is given by the following expression [21]:

$$\Delta f = \frac{2(f_r)^2 \rho_f}{\left(\mu_q \rho_q\right)^{1/2}} \tag{2.17}$$

Where, Δf is the measured frequency shift and ρ_f is the solution film mass density which permits the extraction of the film mass and thickness. The change in frequency due to the added mass is sensitively dependent on the mass sensitivity of the TSM device.

From the Sauerbrey equation, the theoretical mass sensitivity factor of any quartz resonator is defined by:

$$C_f = \frac{2(f_r)^2}{(\mu_q \rho_q)^{1/2}} \tag{2.18}$$

Where f_r is the fundamental-mode resonance frequency. The shear modulus or stiffness of the quartz substrate, μ_q, is 2.947 x 10^{11} g cm^{-1} s^{-2} and the quartz mass density, ρ_q, is 2.648 g cm^{-3} [22]. However, application of a TSM resonator as an organic vapor or film property sensor requires modification of the mass sensitivity factor to account for the increased sensitivity due to the sensing layer, typically thin polymeric films, and the selectivity of that film to organic analyte sorption. An expression for the experimental mass sensitivity factor is derived below [23].

From the Sauerbrey equation the total frequency shift of the TSM device resulting from perturbation of the pure polymer and solvent-loaded polymer film can be separated into the sum of two terms.

$$\Delta f = \Delta f_p + \Delta f_s \tag{2.19}$$

Here, Δf_p and Δf_s are the measured frequency shift associated with the pure polymer film and the solvent, respectively. By establishing the total frequency shift of the resonator as a summation of the shifts resulting from the polymer and solvent, the total areal mass change can be similarly expressed:

$$\Delta m = \Delta m_p + \Delta m_s \tag{2.20}$$

In Equation 2.20, the total areal mass of the solvent-loaded polymer film, Δm, and the areal mass of the pure polymer film, Δm_p, can be defined as:

$$\Delta m = h_f \rho_f \tag{2.21}$$

$$\Delta m_p = h_{f_i} \rho_{f_i} \tag{2.22}$$

Where, h_f and ρ_f are the film thickness and mass density of the solvent-loaded polymer film. The film thickness and mass density of the pure polymer film are h_{f_i} and ρ_{f_i}.

Additionally, the experimental weight fraction of the solvent in the polymer film, w_1, is defined with respect to both mass change and frequency shift:

$$w_1 = \frac{\Delta m_s}{\Delta m_p + \Delta m_s} = \frac{\Delta f_s}{\Delta f_p + \Delta f_s} \tag{2.23}$$

After solving Equation 2.23 for Δm_s and substituting it back into Equation 2.20 along with 2.22, the total areal mass change in terms of the solvent weight fraction becomes:

$$\Delta m = h_{f_i} \rho_{f_i} \left(1 - \frac{w_1}{1 - w_1}\right) \tag{2.24}$$

From Equation 2.24, the experimental mass sensitivity factor of a selective/sensitive film-coated TSM device is:

$$C_{f_e} = \frac{\Delta f_p + \Delta f_s}{h_{f_i}\rho_{f_i}\left(1 - \frac{w_1}{1 - w_1}\right)} \tag{2.25a}$$

or

$$C_{f_e} = \frac{\Delta f_p + \Delta f_s}{h_f \rho_f} \tag{2.25b}$$

Equations 2.25a and 2.25b are a modification of the Sauerbrey model. Using this model, the weight fraction of the solvent and the film thickness of the solvent-loaded polymer film, provided it remains an ideal mass layer, can be measured gravimetrically using a TSM resonator. A discussion of determining the mass density of the solvent-loaded polymer film is given in Section 2.4.2.

In this thesis work, the polymer film is uniformly developed on the surface of the TSM resonator to a thickness beyond that of an ideal mass into the viscoelastic regime meaning the film thickness cannot be monitored gravimetrically. From the polymer/solvent solution thermodynamics derived in Sections 2.3.1 and 2.3.2, the film thickness dynamics of a viscoelastic polymer film upon the sorption of a solvent can be modeled as:

$$h_f = h_{f_i}\left(1 + \frac{\Phi_1}{1 - \Phi_1}\right) \tag{2.26}$$

Equation 2.26 assumes that the polymer swells uniformly upon solvent sorption in a vertical direction within the test cell.

2.4.2 Mixture Density Determination

Another film property that can be measured gravimetrically using a TSM resonator is the change in the mass density of a polymer film due to solvent sorption. This is achieved by following the model algorithm derived in Section 2.4.1. However, as with the film thickness, consideration of the solution thermodynamics is necessary to extract the change in mass density of a viscoelastic solvent-loaded film. The solution mass density of the solvent-loaded polymer film is defined as [24]:

$$\rho_f = \frac{\rho_{f_i} + \mathrm{C}\mathrm{M}_1}{1 + \Phi_1} \tag{2.27}$$

$$\mathrm{C} = \frac{\Phi_1}{V_1^{sat}(1 - \Phi_1)} \tag{2.28}$$

Here, C is a concentration expressing the molar amount of solvent per volume of polymer.

2.5 Viscoelastic Shear Moduli Extraction

Given the difficulty to directly observe and characterize the dynamic behavior of a perturbated viscoelastic film on the resonator surface, it is possible to determine the effect the film has on the electrical and mechanical properties of the resonator. A mechanical coupling between the shear displacement across the film and the electric field in the quartz substrate, established when a axial voltage load is put across a piezoelectric substrate, causes a significant change in the response of the TSM resonator [25]. The near-resonance electrical characteristics of the unperturbed and film-coated resonator can be modeled through an equivalent circuit analysis. From the equivalent circuit model, a combined mechanical impedance/film perturbation model can be established to

accurately extract the storage, *G'*, and loss, *G''*, moduli of a pure polymer or solvent-loaded polymer viscoelastic film [4, 9, 26].

2.5.1 Butterworth-Van Dyke (BVD) Equivalent Circuit

To model or simulate the near-resonance electrical characteristics of a TSM resonator coated with a viscoelastic film, the Butterworth-Van Dyke (BVD) equivalent circuit can be used [27]. The equivalent circuit is established through a simple lumped-element electrical analysis of the TSM resonator. These lumped-elements can be directly correlated to the physical properties of the substrate and a deposited film. Within the circuit for the uncoated resonator, there are two branches, a static branch consisting of a static capacitance, C_o, and a motional branch that results from the electro-mechanical coupling indicative of an excited piezoelectric substrate. The motional branch introduces a circuit resistance, R_1, attributed to the energy loss in the substrate, an inductance, L_1, from friction loss, and a capacitance, C_1, from the quartz mechanical elasticity. Figure 2.3 is a schematic of a BVD circuit representing a perturbed and unperturbed TSM resonator. The above electrical elements are defined as follows [20].

$$C_o = \frac{\epsilon_{22} A}{h_q} \tag{2.29}$$

$$C_1 = \frac{8K^2 C_o}{(N\pi)^2} \tag{2.30}$$

$$L_1 = \frac{1}{\omega_s{}^2 C_1} \tag{2.31}$$

$$R_1 = \frac{\eta_q}{\bar{c}_{66} C_1} \tag{2.32}$$

Here, A and h_q are the area of the electrode and thickness of the quartz substrate. K, ϵ_{22}, η_q, and $\bar{c}_{66}$ are the quartz electro-mechanical coupling coefficient, dielectric permitivity, effective viscosity, and shear stiffness, respectively. The coefficient N corresponds to the harmonic resonance mode with N = 1 being the fundamental mode. Angular frequency of the bare quartz, ω_s, is defined as $\omega_s = 2\pi f_r$ where f_r is the series resonant frequency. A mass loading coupled to the resonator surface contributes additional motional elements to the equivalent circuit which are represented by a series-motional resistance, R_2, and inductance, L_2, in Figure 2.3. These electrical parameters are defined and discussed in Section 2.5.2.

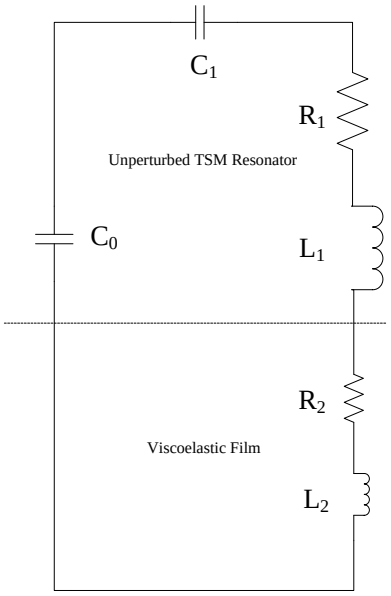

Figure 2.3: BVD equivalent circuit representing the unperturbed and perturbed TSM resonator.

2.5.2 Combined Mechanical Impedance and Film Perturbation Model

To connect the physical properties of a viscoelastic film to the electrical and mechanical response of the resonator requires the establishment of a motional mechanical impedance model based on the above equivalent circuit. Deposition of a viscoelastic film

induces an increase in the motional impedance at the film/substrate interface introducing a complex load impedance, Z_e. This complex load impedance relates the shear wave characteristic impedance of the quartz, Z_q, to the shear mechanical surface impedance transmitted from the film, Z_s [9, 22, 26].

$$Z_e = \frac{N\pi}{4K^2\omega_s C_0}\left(\frac{Z_s}{Z_q}\right) \tag{2.33}$$

$$Z_q = \left(\rho_q \mu_q\right)^{1/2} \tag{2.34}$$

The expression for the surface impedance contributed from the film is derived by assuming the steady-state sinusoidal shear stress, T_{xy}, acting on the film at the surface center of the resonator is indirectly proportional to the surface particle velocity, v_x [22]. See Figure 2.1 for the Cartesian coordinate placement.

$$Z_s = \left.\frac{T_{xy}}{v_x}\right|_{y=0} \tag{2.35}$$

Noting that Equation 2.35 yields a complex quantity, Z_e can be expressed in complex form in terms of the motional equivalent circuit elements contributed from the film, R_2 and L_2 [26].

$$Z_e = R_2 + j\omega_s L_2 \tag{2.36}$$

Combining Equations 2.33 and 2.36 results in direct expressions for R_2 and L_2.

$$R_2 = \frac{N\pi}{4K^2\omega_s C_0}\left(\frac{Re(Z_s)}{Z_q}\right) \tag{2.37}$$

$$L_2 = \frac{N\pi}{4K^2{\omega_s}^2 C_0}\left(\frac{Im(Z_s)}{Z_q}\right) \tag{2.38}$$

Considering a TSM resonator that is only coated with a finite-thickness viscoelastic film, a model for the shear mechanical impedance, Z_s, at the resonator/film interface can be written with respect to the complex shear modulus of the viscoelastic film, *G*. This model is derived from a transmission line theory applied to a viscoelastic film-coated TSM resonator [28].

$$Z_s = jZ_0 tan\left[\omega_s\left(\frac{\rho_f}{G}\right)^{1/2} h_f\right] \tag{2.39}$$

Where, Z_0 is the characteristic impedance of the viscoelastic film and denoted as $\left(\rho_f G\right)^{1/2}$. Due to the complex nature of the film shear modulus, *G*, a precise approximation of Equation 2.39 must be used to further develop the impedance model in order to directly extract the storage, *G′*, and loss, *G″*, moduli. A Taylor series expansion of the tangent function, retaining the first three terms, provides an adequate approximation [29].

$$tan\left[\omega_s\left(\frac{\rho_f}{G}\right)^{1/2} h_f\right] \approx \omega_s h_f\sqrt{\frac{\rho_f}{G}} + \frac{1}{3}{\omega_s}^3{h_f}^3\left(\frac{\rho_f}{G}\right)^{3/2} + \frac{2}{15}{\omega_s}^5{h_f}^5\left(\frac{\rho_f}{G}\right)^{5/2} \tag{2.40}$$

From the Taylor series expansion, Z_s becomes:

$$Z_s \approx j(\rho_f G)^{1/2}\left[\omega_s h_f\sqrt{\frac{\rho_f}{G}}+\frac{1}{3}{\omega_s}^3{h_f}^3\left(\frac{\rho_f}{G}\right)^{3/2}+\frac{2}{15}{\omega_s}^5{h_f}^5\left(\frac{\rho_f}{G}\right)^{5/2}\right] \tag{2.41}$$

Upon separation of the real and imaginary parts in Equation 2.41 and decomposition, Z_s is rewritten as [4]:

$$\begin{aligned} Z_s = {} & \frac{{\omega_s}^3{h_f}^3{\rho_f}^2}{3}\frac{G''}{|G|^2}+\frac{4{\omega_s}^2{h_f}^5{\rho_f}^3}{15}\frac{G'G''}{|G|^4} \\ & + j\omega_s\left(h_f\rho_f+\frac{{\omega_s}^2{h_f}^3{\rho_f}^2}{3}\frac{G'}{|G|^2}+\frac{2{\omega_s}^4{h_f}^5{\rho_f}^3}{15}\frac{(G')^2}{|G|^4}\right. \\ & \left. -\frac{2{\omega_s}^4{h_f}^5{\rho_f}^3}{15}\frac{(G'')^2}{|G|^4}\right) \end{aligned} \tag{2.42}$$

Substitution of Equation 2.42 into 2.33 provides an analytical expression for the complex load impedance, Z_e, in terms of G' and G''.

$$\begin{aligned} Z_e = {} & \frac{N\pi}{4K^2\omega_s C_0}\frac{1}{\sqrt{\rho_q\mu_q}}\left[\frac{{\omega_s}^3{h_f}^3{\rho_f}^2}{3}\frac{G''}{|G|^2}+\frac{4{\omega_s}^2{h_f}^5{\rho_f}^3}{15}\frac{G'G''}{|G|^4}\right. \\ & + j\omega_s\left(h_f\rho_f+\frac{{\omega_s}^2{h_f}^3{\rho_f}^2}{3}\frac{G'}{|G|^2}+\frac{2{\omega_s}^4{h_f}^5{\rho_f}^3}{15}\frac{(G')^2}{|G|^4}\right. \\ & \left.\left. -\frac{2{\omega_s}^4{h_f}^5{\rho_f}^3}{15}\frac{(G'')^2}{|G|^4}\right)\right] \end{aligned} \tag{2.43}$$

Using Equation 2.36, reduction of Equation 2.43 into explicit expressions for the film storage, *G'*, and loss, *G''*, moduli is possible [4, 26].

$$G' = \frac{B}{A^2 + B^2} \tag{2.44a}$$

$$G'' = \frac{A}{A^2 + B^2} \tag{2.44b}$$

Where,

$$A = \left(\frac{\frac{19 h_f \rho_f}{24} - \frac{L_2}{A_0} + \left[\left(\frac{L_2}{A_0} - \frac{19 h_f \rho_f}{24} \right)^2 + \frac{{R_2}^2}{{\omega_s}^2 {A_0}^2} \right]^{1/2}}{\frac{4 {\omega_s}^4 {h_f}^5 {\rho_f}^3}{15}} \right)^{1/2} \tag{2.44c}$$

$$B = \frac{15 R_2}{4 {\omega_s}^5 {h_f}^5 {\rho_f}^3 A_0 A} - \frac{5}{4 {\omega_s}^2 {h_f}^2 \rho_f} \tag{2.44d}$$

$$A_0 = \frac{N\pi}{4K^2 \omega_s C_0} \frac{1}{\sqrt{\rho_q \mu_q}} \tag{2.44e}$$

Employing either an impedance or network analyzer, admittance data obtained for the perturbed and unperturbed resonator are fitted to the BVD equivalent circuit model and the electrical elements determined [9]. From these elements, namely R_2 and L_2, the storage, *G'*, and loss, *G''*, moduli of a pure or solvent-loaded viscoelastic film can be extracted.

2.6 Fractional Free-Hole Volume Extraction

Extraction of the fractional free-hole volume of a pure polymer or solvent-loaded polymer viscoelastic film is possible provided that the viscoelastic shear moduli, *G*, is known for the film under the respective system conditions. The extraction method is provided in this section along with an accurate FV model for correlation.

2.6.1 Superposition Principle

The storage, *G'*, and loss, *G''*, moduli of a pure poly(isobutylene) viscoelastic film at 293.15 K under various oscillation frequencies was studied by Ferry and are given in Figure 2.4. [3].

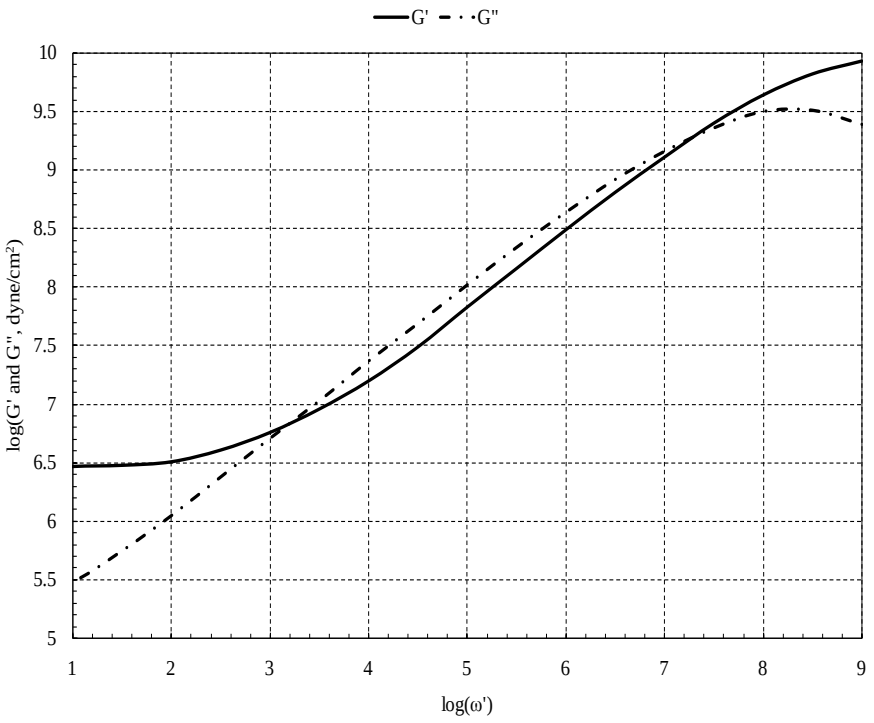

Figure 2.4: Storage, *G'*, and loss, *G''*, moduli of a pure poly(isobutylene) film versus apparent oscillation frequency.

From the "master curves" in Figure 2.4, a superposition principle can be applied to equate the shear moduli of a pure poly(isobutylene) film at 293.15 K to that of a poly(isobutylene) film resonating at a different frequency, at another system temperature, or subjected to solvent sorption [24, 30].

$$log(\omega') = log(\omega) + log(a_T) \tag{2.45}$$

Where, ω' and ω are the apparent probe angular frequencies of the pure PIB film at 293.15 K and a film at different system conditions, respectively. The translation in the polymer relaxation time is given by a_T.

2.6.2 Doolittle Equation

The shift factor, a_T, relating the storage, *G'*, and loss, *G''*, moduli of complementary viscoelastic polymer films can be expressed in terms of the fractional free-hole volume using the well known Doolittle equation. Similar to the Williams-Landel-Ferry (WLF) model [31], the general Doolittle equation accounts for the effects of temperature on the polymer free volume in terms of a_T and is given as followed [32].

$$log(a_T) = \frac{B}{2.303}\left(\frac{1}{f} - \frac{1}{f_o}\right) \tag{2.46}$$

Here, *B* is the Doolittle constant and is taken as unity (*B* = 1). The fractional free-hole volume of a polymer film at a reference temperature, T_o, is given by f_o.

For a polymer film at a temperature above its glass transition temperature, T_g, the fractional free-hole volume, f, can be expressed as:

$$f(T℃) = f_o + \alpha_f[T℃ - T_o℃] \tag{2.47}$$

Where, α_f is the thermal expansion coefficient of a polymer averaged over a wide-range of temperatures. Model parameters for poly(isobutylene) are tabulated in Table 2.5.

Table 2.5: Doolittle equation parameters for poly(isobutylene)

Parameter	Value
$T_g, (K)$	205
$\alpha_f, (1/℃)$	2.5 x 10^{-4}
$T_o, (K)$	293.15
f_o	0.05
Reference	[24]

The Doolittle equation can be extended to account for solvent-sorption effects on the fractional free-hole volume of a polymer film:

$$log(a_T) = -\frac{B}{2.303}\left[\frac{\alpha_f[T℃ - T_o℃] + \chi\Phi_1}{f_o + \alpha_f[T℃ - T_o℃] + \chi\Phi_1}\right] \tag{2.48}$$

Where, Φ_1 is the volume fraction of the solvent in the polymer film (see Section 2.3.2).

The empirical plasticizing parameter, χ, represents the solvent effect on polymer free volume.

$$f(T°\text{C}, \Phi_1) = f(T°\text{C}) + \chi\Phi_1 \tag{2.49}$$

Using storage, *G'*, and loss, *G''*, moduli data determined using a TSM resonator for the poly(isobutylene)/solvent systems considered in this study, experimental fractional free-hole volume as a function of solvent concentration can be extracted from the superposition principle and modified Doolittle equation.

2.6.3 Vrentas-Duda Free-Volume (FV) Theory

Correlation of experimental fractional free-hole volume of polymer/solvent systems can be accomplished reliably using available FV-based equations of state (EOS) that are derived from lattice-fluid theory including the Sanchez-Lacombe (SL) EOS [33] and the Simha-Somcynsky (SS) model [34], as well as, empirical models which incorporate free volume properties of pure associating fluids. An example of an empirical model is the Vrentas-Duda FV model. The Vrentas-Duda FV model is given by [35, 36]:

$$\frac{\hat{V}_f}{\gamma} = w_1 \frac{K_{11}}{\gamma_1}\left(T + K_{21} - T_{g_1}\right) + w_2 \frac{K_{12}}{\gamma_1}\left(T + K_{22} - T_{g_2}\right) \tag{2.50}$$

Where, $\frac{\hat{V}_f}{\gamma}$ is defined as the total available free-hole volume of the system per gram of polymer. Determined from temperature-pressure viscosity data for a pure fluid, K_{11} and K_{21} are the solvent free volume parameters. For the pure polymer, the parameters are K_{12} and K_{22}. Glass transition temperatures of the solvent and polymer are represented by T_{g_1} and T_{g_2}, respectively. The fractional free-hole volume of the polymer/solvent system

is found by multiplying Equation 2.50 by the solution mass density. Free volume parameters for the poly(isobutylene)/solvent systems considered in this work are tabulated in Table 2.6.

Table 2.6: Vrentas-Duda FV model parameters for poly(isobutylene)/solvent systems

Solvent	Benzene	Chloroform	n-Hexane	Dichloromethane
$K_{11}/\gamma_1, (cm^3/g-K)$	1.51 x 10^{-3}	7.12 x 10^{-4}	1.96 x 10^{-3}	1.05 x 10^{-3}
$K_{12}/\gamma_2, (cm^3/g-K)$	3.16 x 10^{-4}	3.16 x 10^{-4}	3.16 x 10^{-4}	3.16 x 10^{-4}
$K_{21}-T_{g1}, (K)$	-94.32	-29.43	-41.08	-62.0
$K_{22}-T_{g2}, (K)$	-117.93	-117.93	-117.93	-117.93
Reference	[6]	[6]	[6]	[37]

CHAPTER 3

TSM QUARTZ RESONATOR BASED MASS NANOBALANCE

3.1 Introduction

Development and testing of a modified electrode TSM resonator that exhibits a uniform mass sensitivity profile over a large active area is presented in this thesis work for the purpose of producing an absolute nanobalance. An absolute TSM-based nanobalance should permit the mass measurement of any mass loading regardless of placement within the active area of the resonator. Commercially available TSM resonators are capable of measuring mass loadings to nanogram precision, however, their non-uniform mass sensitivity profile limits the mass characterization to uniform films. The advent of a practical and robust nanobalance would revolutionize the mass characterization industry and reduce reliance on mechanical/analytical mass balances which are expensive, limited to microgram sensitivity, and vulnerable to considerable mechanical vibration instability. A study of the effects of simple electrode geometries on the mass sensitivity of TSM resonators and an optimized electrode design predicted to generate a uniform mass sensitivity distribution are discussed in this section.

3.2 Mass Sensitivity of TSM Quartz Resonators

Extensive analytical and experimental studies of TSM resonators have indicated that the mass sensitivity is heavily dependent on both the electrode and quartz surface geometries [38, 39]. The profile or shape of the mass sensitivity is attributed to the electrode geometry, whereas, the broadness of the distribution is set by the contour of the quartz surface. Therefore, to manipulate the mass sensitivity distribution, consideration of the electrode design is necessary. The electrodes considered in this study are an 'n-m' design consisting of two equivalent-diameter circular electrodes deposited on either face of the quartz substrate (the electrode configuration of current TSM resonators) and a single ring electrode on the top face with a circular electrode on the bottom. Figure 3.1 illustrates these electrode designs.

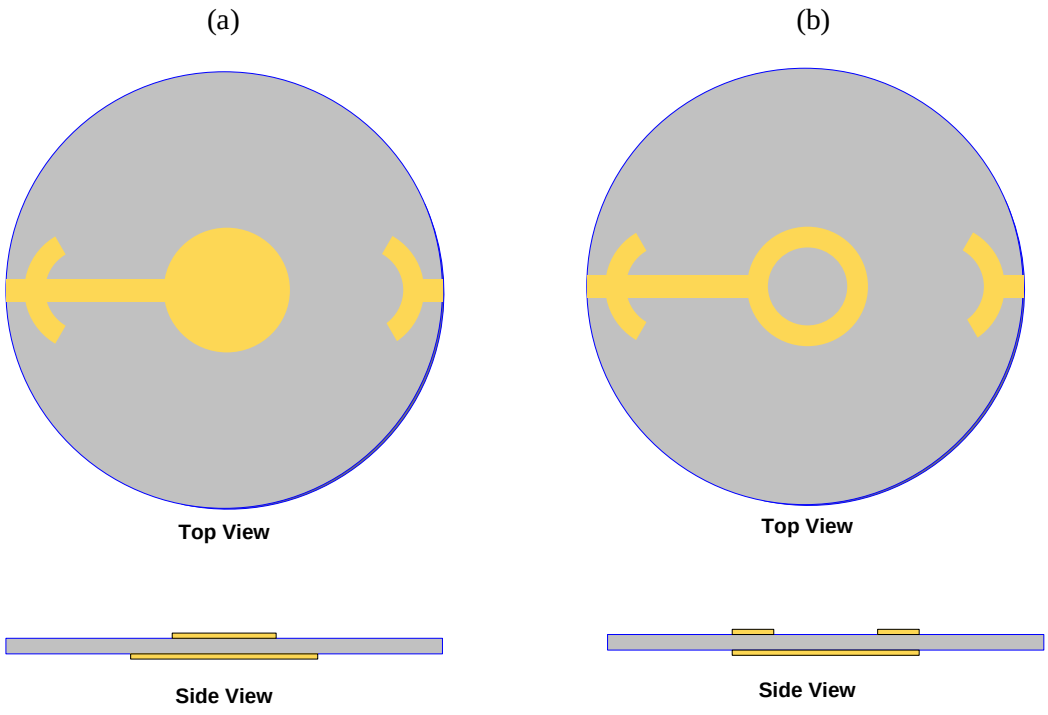

Figure 3.1: Simple electrode designs for a TSM quartz resonator: (a) solid 'n-m' electrode configuration, and (b) single ring electrode configuration.

Non-uniformity in mass sensitivity across the surface plane of current TSM devices is well documented [1, 2, 38, 40, 41]. This non-uniformity is attributed to the reduction in particle displacement amplitude extending from the center. At the device center, the resonating wave drives the quartz from all radial directions prompting maximum displacement and, consequently, mass sensitivity. Moving away from the center, the displacement amplitude tapers off with radial position producing a Gaussian-like distribution in the mass sensitivity, depicted by the distribution for the 'n-m' electrode design in Figure 3.2. The mass sensitivity distributions in Figure 3.2 were generated using the analytical models in Ref. [42].

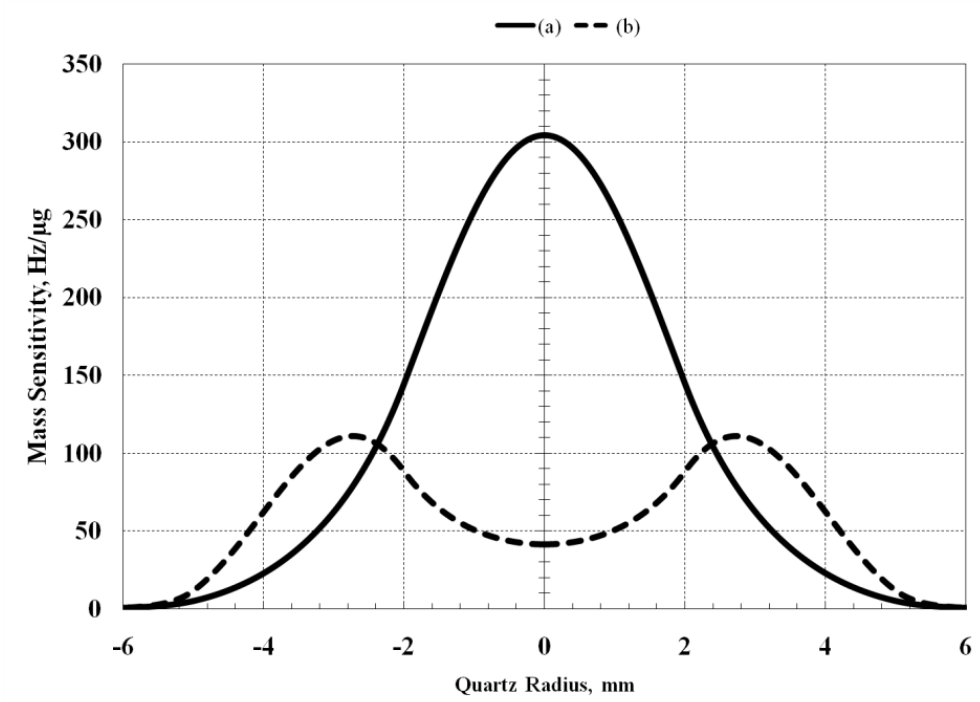

Figure 3.2: Mass sensitivity distributions for simple electroded 5 MHz TSM resonator: (a) 'n-m' electrode configuration with top and bottom diameters of 4 and 10 mm, respectively, with R = 0.0036 and (b) ring electrode configuration with inner and outer diameters of 4 and 10 mm, respectively, with R = 0.0334.

Additional contributions to the non-uniformity of the mass sensitivity arise from the anisotropic structure of the quartz. Observed deviations in sensitivity measurements from other studies, sweeping multiple radial axes of the resonator from $\theta = 0°$ to $90°$, indicates that the wave propagation characteristics are notably different depending on the axis of motion in the quartz substrate [41]. Although the studies were not explicitly driven towards reducing the effects of the anisotropy of piezoelectric substrates on the wave propagation and mass sensitivity profile, previous research has considered alternative quartz surface geometries including plano-convex, with the top face of the crystal convexly contoured and the bottom remaining planner, to eliminate the destructive coupling observed between the fundamental and flexural (parasitic) oscillating modes in plano-plano devices. Cancellation of the fundamental operating mode by these flexural modes upon the deposition of electrode mass on the plano-plano resonator device dampens the energy of the resonator prompting a lower quality factor, Q [39]. The decoupling of these modes for electroded plano-convex surfaces forces all of the energy of the driving acoustic wave to the center with minimal energy trapping extending out to the crystal edge. As a result, the Q-factor and mass sensitivity is higher, by a factor of two, for the plano-convex resonator compared to the plano-plano [41]. Reduction of the anisotropic effects would be observed using the plano-convex surface with the concentration of the energy within a small active area at the center of the resonator. However, an increase in Q-factor prompts a narrowing of the mass sensitivity distribution which would make achieving a uniform mass sensitivity distribution potentially difficult. The broad-distribution indicative of the plano-plano quartz resonator is inherently capable of producing the bimodal profile necessary to achieve uniformity over a large sensing area.

3.3 Theoretical Modeling of the Mass Sensitivity Profile for Simple Electroded TSM Resonators

Development of analytical mathematical models for predicting the mass sensitivity of TSM devices having simple electrode configurations has continued since

Sauerbrey's initial study of the frequency shift due to mechanical loading on the device surface. Typically, these models are generated through either a resonant frequency analysis or three-dimensional perturbation modeling of the wave motion in the quartz substrate. However, these techniques share a common assumption that the mass sensitivity is proportional to the square of the quartz particle displacement amplitude [38, 43-45]. In this study, a model is employed that is based upon a resonance analysis across the sensor platform, which is capable of producing displacement amplitude distributions for the 'n-m' and ring electrode designs shown in Figure 3.1 [38].

As mentioned previously, the radial mass sensitivity profile of a TSM device is predominantly influenced by the electrode configuration. From previous analytical studies of the mass sensitivity of a ring electrode TSM resonator, it is known that the sensitivity profile exhibits a bimodal response across the resonator surface (See Figure 3.2) [38, 42]. The ability to establish a uniform mass sensitivity distribution over a large active area is less difficult when dealing with a bimodal response compared to a Gaussian-like response in mass sensitivity. Therefore, the analytical model for mass sensitivity for the ring electrode case is considered in this work and derived below [42].

Mechanical mass sensitivity for any TSM quartz resonator, $S_f(r)$, as a function of the quartz radius, is governed by the particle displacement amplitude, $\hat{u}_1(r)$, resulting from the shear horizontal wave propagating through the quartz substrate.

$$S_f(r) = \frac{|\hat{u}_1(r)|^2}{2\pi \int_0^\infty r|\hat{u}_1(r)|^2 dr} \tag{3.1}$$

By assuming the resonator to be a cylindrical system, the particle displacement amplitude across the resonator surface can be represented by a scalar Helmholtz wave equation [46].

$$r^2 \frac{\partial^2 \hat{u}_1(r,\theta)}{\partial r^2} + r \frac{\partial \hat{u}_1(r,\theta)}{\partial r} + \frac{\partial^2 \hat{u}_1(r,\theta)}{\partial \theta^2} + (rk_r)^2 \hat{u}_1(r,\theta) = 0 \tag{3.2}$$

Where, k_r is a wave propagation constant set by resonance boundary conditions across the resonator surface. These boundary conditions for a ring electrode device are the partially electroded region located between the resonator center and the inner ring radius, *a*, the fully electrode region, between the inner and outer ring radii, *a* and *b*, and the un-electroded region, from *b* to the edge of the resonator. Figure 3.3 depicts these regions. For each of these regions, k_r is defined as:

$$k_r = \begin{cases} \frac{\pi^2}{4{h_q}^2} \frac{1}{{f_{66}}^2} \left(f^2 - {f_{ce}}^2\right) & 0 \le r \le a \\ \frac{\pi^2}{4{h_q}^2} \frac{1}{{f_{66}}^2} \left(f^2 - {f_{cp}}^2\right) & a \le r \le b \\ \frac{\pi^2}{4{h_q}^2} \frac{1}{{f_{66}}^2} \left(f^2 - {f_{cu}}^2\right) & b \le r < \infty \end{cases} \tag{3.3}$$

Here, f is the operating frequency of the resonator and f_c is the cutoff frequency in each electroded region. Equations for the cutoff frequencies are presented in Appendix A. The thickness of the quartz substrate, which is dependent on the resonance frequency of the TSM resonator, is given by h_q.

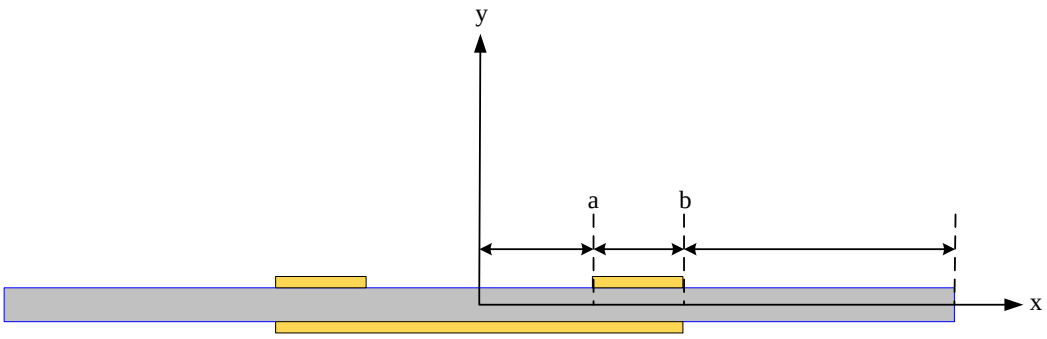

Figure 3.3: Electroded regions across a ring electrode TSM resonator.

Operation of a TSM resonator in the fundamental operating mode results in the particle displacement being invariant with angular direction, θ, and only dependent on radial placement across the resonator surface [38]. Therefore, Equation 3.2 can be rewritten as:

$$r^2 \frac{\partial^2 \hat{u}_1(r)}{\partial r^2} + r \frac{\partial \hat{u}_1(r)}{\partial r} + (rk_r)^2 \hat{u}_1(r) = 0 \tag{3.4}$$

Taking the form of a Bessel function differential equation, the solution of Equation 3.4 becomes:

$$\hat{u}_1(r) = \begin{cases} AJ_0(rk_r) + BN_0(rk_r) & (rk_r)^2 > 0 \\ AI_0(rk_r) + BK_0(rk_r) & (rk_r)^2 > 0 \end{cases} \tag{3.5}$$

Applying the boundary conditions of the ring electrode TSM resonator and properties of Bessel functions [47], the exact solution for the particle displacement amplitude for the ring electrode resonator is:

$$\hat{u}_1(r) = \begin{cases} AI_0\left(k_r^p r\right) & 0 \le r \le a \\ BJ_0(k_r^e r) + CN_0(k_r^e r) & a \le r \le b \\ DK_0(k_r^u r) & b \le r < \infty \end{cases} \tag{3.6}$$

To solve for the amplitude constants, *A, B, C,* and *D,* a set of homogeneous equations can be derived from Equation 3.6 by assuming the following continuity conditions [38].

Continuity Conditions:

i). $\hat{u}_1(a) = \hat{u}_1(b)$

ii). $\frac{\partial \hat{u}_1(r)}{\partial r}\Big|_{r=a} = \frac{\partial \hat{u}_1(r)}{\partial r}\Big|_{r=b}$

From these conditions, the set of homogeneous equations are:

$$\begin{bmatrix} I_0\left(k_r^p a\right) & -J_0(k_r^e a) & -N_0(k_r^e a) & 0 \\ k_r^p I_1\left(k_r^p a\right) & k_r^e J_1(k_r^e a) & k_r^e N_1(k_r^e a) & 0 \\ 0 & J_0(k_r^e b) & N_0(k_r^e b) & -K_0(k_r^u a) \\ 0 & -k_r^e J_1(k_r^e b) & -k_r^e N_1(k_r^e b) & k_r^u K_1(k_r^u b) \end{bmatrix} \begin{bmatrix} A \\ B \\ C \\ D \end{bmatrix} = 0 \tag{3.7}$$

Here, *I, J, N,* and *K* are Bessel functions with the subscripts denoting the zeroth and first kind. The amplitude constants are calculated by finding the non-trivial solutions for the equation set in Equation 3.7. Finding the non-trivial solutions is achieved by determining the adjoint of the coefficient matrix. With the amplitude constants known, the particle displacement profile across the resonator surface can be resolved.

However, to generate the mass sensitivity profile, a definite solution to the integral in the numerator of Equation 3.1 is required. A definite integral is obtained by squaring Equation 3.6, shown below in Equation 3.8, and taking an integral over the boundary conditions. The integral is given in Equations A.7 through A.10 in Appendix A.

$$|\hat{u}_1(r)|^2 = \begin{cases} A^2 {I_0}^2(k_r^p r) & 0 \le r \le a \\ B^2 {J_0}^2(k_r^e r) + C^2 {N_0}^2(k_r^e r) + 2BCJ_0(k_r^e r)N_0(k_r^e r) & a \le r \le b \\ D^2 {K_0}^2(k_r^u r) & b \le r < \infty \end{cases} \tag{3.8}$$

From this model, the mass sensitivity profile for a simple ring electrode TSM resonator having any dimensions and electrode mass loading factor, *R*, can be predicted. The electrode mass loading factor is the ratio of the overall electrode areal mass, $\rho_e h_e$, to that of the quartz substrate, $\rho_q h_q$. This is an important term in that it sets the magnitude of the maximum mass sensitivity of the TSM resonator and the extent to which the mass sensitivity tapers toward the center of a ring electrode resonator (See Figure 3.2).

$$R = \frac{\rho_e h_e}{\rho_q h_q} \tag{3.9}$$

3.4 Optimization of Electrode Design

To fabricate and test a TSM resonator that exhibits a uniform mass sensitivity distribution over a large active area requires modification and optimization of the electrode configuration. Utilizing computations based upon the analytical modeling in Section 3.3, it can be shown that electrode mass loading factors, *R*, exist which can theoretically produce uniform mass sensitivity distributions for many ring electrode configurations. For example, with a ring electrode having inner and outer diameters of 4 and 10 mm, respectively, a uniform mass sensitivity profile over a large active area is produced at an *R* value of 0.0025 which corresponds to Cr/Au electrode thicknesses of 75

Å and 1050 Å, respectively. Figure 3.4 shows the effect of varying the *R* value from 0.0025 to 0.0088 on the mass sensitivity profile of a 5 MHz resonator with a 4-10 mm ring electrode.

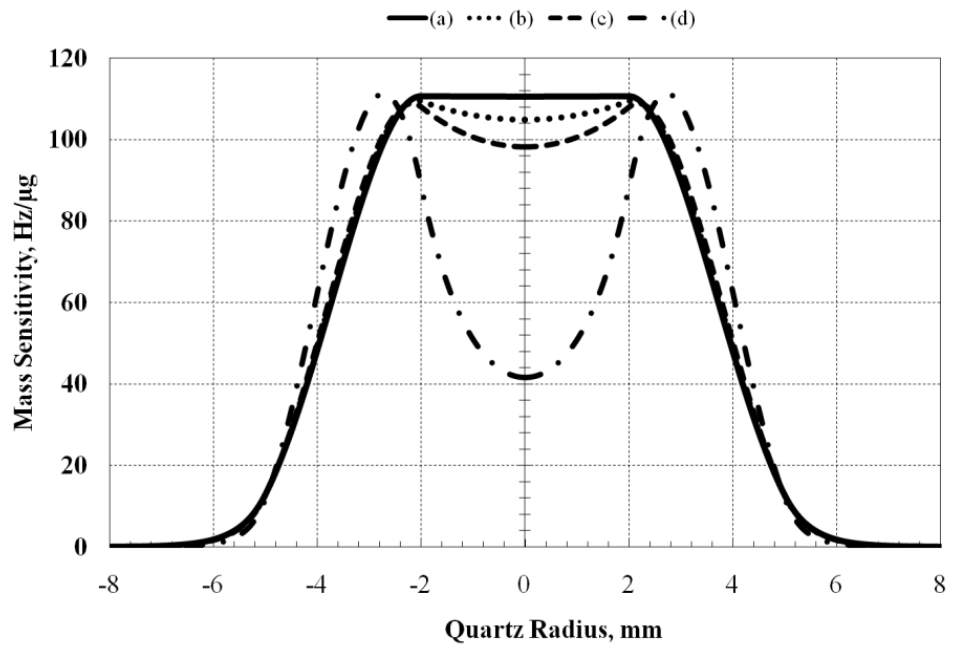

Figure 3.4: Mass sensitivity distributions for a ring electrode 5 MHz TSM resonator having inner and outer diameters of 4 and 10 mm, respectively, with: (a) R = 0.0025, (b) R = 0.0033, (c) R = 0.0042, and (d) R = 0.0088.

Based on the findings above, 4-10 mm ring electrode 5 MHz TSM resonators were fabricated and tested in this work to verify the establishment of a uniform mass sensitivity profile. Although these ring electrode design parameters do indeed theoretically produce a uniform sensitivity distribution, it should be noted that the maximum sensitivity is considerably less, one order of magnitude, than commercially available 5 MHz 'n-m' electrode TSM devices. The reduced mass sensitivity of the ring electrode design results from the confinement of both the excited acoustic wave and the energy associated with the driving wave within the fully electroded region, between the ring radii *a* and *b* [38]. All the same, the mass sensitivity of the proposed ring design is sufficient for most nanogram mass detection applications.

3.5 Droplet Gravimetry of Non-Volatile Residue (NVR) in Solvents

A major industrial application that would benefit from the advent of a TSM based nanobalance is the measurement of non-volatile residue (NVR) in high-purity solvents [48, 49]. Required by law, solvent producers must report the level of NVR in each batch of purified solvent that is sold. A current method to characterize NVR per volume of solvent involves a thermal gravimetric technique where a large quantity of solvent is evaporated and the remnant NVR weighed in a mechanical/analytical balance. This process is both expensive and time consuming. Fortunately, a TSM resonator that exhibits a uniform mass sensitivity distribution would enable the determination of NVR in solvents by droplet gravimetry where only a nanogram droplet is needed for measurement. The experimental process of droplet gravimetry is given in Section 4.3.

CHAPTER 4

EXPERIMENTAL PREPARATIONS AND PROCEDURES

4.1 Viscoelastic Shear Modulus Measurements

Section 4.1 provides details of the experimental technique to measure the viscoelastic shear moduli of poly(isobutylene)/solvent systems including the process of organic vapor generation, polymer film preparation and deposition on the resonator surface, the overall experimental apparatus, and procedure.

4.1.1 Vapor Generation

Generation of the necessary organic solvent vapors is achieved using a specially designed dilution system [10, 23]. Contained in a bubbler flask, the solvent is cooled to the desired saturation temperature, in this case 288.15 K, by circulating water surrounding the flask. The water temperature is maintained using a calibrated water bath (Lauda Heater/Chiller Water Circulator). It should be noted that the chosen saturation temperature is well below the system temperature, 298.15 K, to ensure that the generated vapor does not condense. After cooling, the solvent is charged with a certain flow rate of pure nitrogen (UHP grade, Airgas) forcing it to vaporize at a vapor pressure corresponding to the saturation temperature. This pressure is approximated well by the Wagner equation which is discussed in Section 2.3.1. The resulting vapor is further diluted downstream by two pure nitrogen streams to the desired concentration and delivered to the TSM resonator test cell. To achieve increasing solvent vapor

concentration, the flow of nitrogen entering the bubbler is increased while the dilution streams are decreased; however, the total nitrogen flow is kept at a constant 100 sccm. Nitrogen flow is maintained using a series of mass flow controllers, relays, and Teflon-reinforced solenoid valves. The dilution system is capable of producing organic vapor in nitrogen to partial pressures ranging from 0 to 100 % of the vapor pressure. Figure 4.1 presents the dilution system configuration.

4.1.2 Polymer Film Preparation

The polymer poly(isobutylene), (PIB), with a reported mass-average molecular weight of 420K, was obtained from Sigma-Aldrich Chemical Co. and used as received. To achieve the necessary film coating for the measurement of the viscoelastic shear modulus of pure PIB and solvent-loaded PIB viscoelastic films using a TSM resonator, the polymer was dissolved in chloroform to a solution concentration of 7.0 % by-weight. Using a spin-coater (Laurell Tech.) to ensure uniform coating, the PIB film was spun-casted at 3500 rpm for 35 seconds on the surface 1-inch diameter 5 MHz TSM quartz resonator. After annealing in a vacuum oven at 90ºC in a vacuum oven at a pressure of 25 in Hg for one hour, the film thickness was measured by profilometry to be approximately 13.0 ± 0.2 μm, an appropriate thickness for a pure PIB film to exhibit viscoelastic tendencies [9].

4.1.3 Experimental Apparatus

A combined schematic of the vapor dilution system and the TSM resonator testbed is given in Figure 4.1. Details of the function of each component are incorporated in the experimental procedure given in Section 4.1.4.

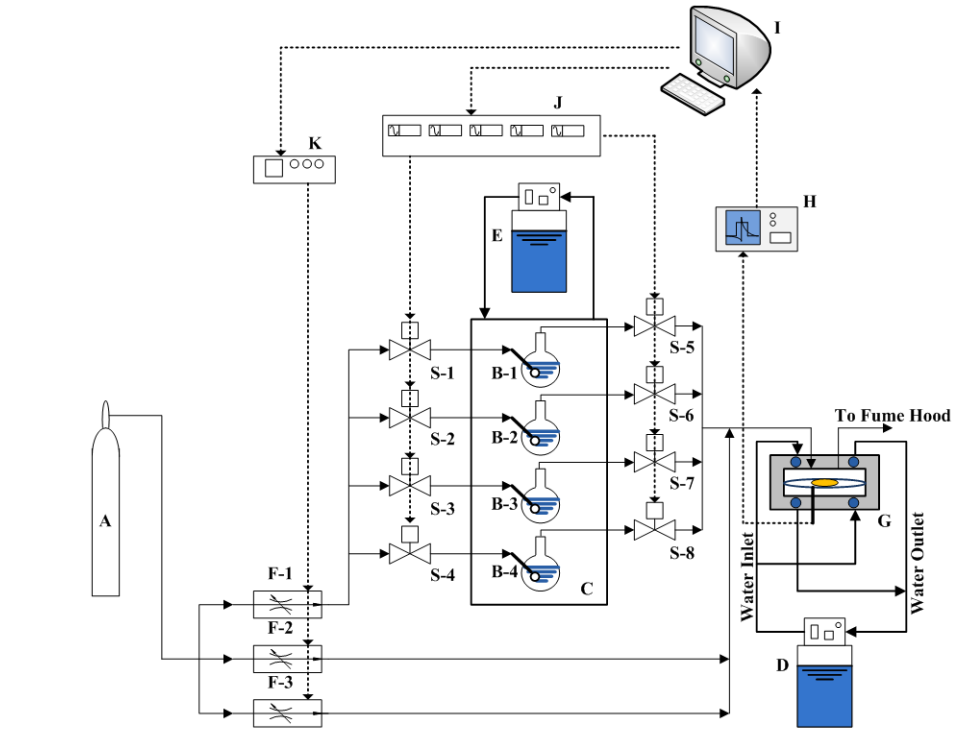

A – Nitrogen Cylinder
B-1-4 – Vapor Generator Units
C – Water Bath
D – Thermo Neslab RTE 740 Heater/Chiller Water Circulator
E – Lauda Heater/Chiller Water Circulator
F-1 – MKS Mass Flow Controller (Carrier Gas)
F-2 – MKS Mass Flow Controller (Dilutant 1)

F-3 – MKS Mass Flow Controller (Dilutant 2)
G – TSM Resonator Stainless-Steel Test Cell
H – Agilent 4294A Impedance Analyzer
I – Computer Workstation
J – Relay Junction
K – MKS Mass Flow Meter
S-1-8 – Solenoid Valves

Figure 4.1: Experimental apparatus for vapor generation apparatus and TSM resonator testing.

4.1.4 Experimental Procedure

The technique for determining the viscoelastic shear moduli of PIB and solvent-loaded PIB viscoelastic films using a TSM resonator is described by the following procedure. A 1-inch diameter polished Cr/Au 5 MHz TSM AT-cut quartz resonator was obtained (Inficon, formerly Maxtek, Inc.) and cleaned using a solvent rinse (acetone/methanol/isopropanol) and plasma-cleaner (Harrick, model PDC-23G). After a

thorough cleaning, the resonator was placed in a specially designed stainless steel test cell with drilled channels allowing heated water circulation for maintaining the desired system temperature, in this case 298.15 K. Using an impedance analyzer (Agilent, model 4294A), the frequency and admittance data for the bare TSM resonator were recorded. The impedance analyzer has a built-in regression algorithm for fitting the admittance data to the BVD equivalent circuit discussed in Section 2.5.1 allowing the real-time measurement of the equivalent circuit elements of the resonator. With the bare crystal electrical parameters known, the resonator was removed from the test cell and coated with a viscoelastic PIB film as discussed in Section 4.1.2. The coated resonator was then placed back in the test cell and allowed to stabilize at the system temperature. Upon stabilization, monitored by observing the resonant frequency of the perturbed resonator, the added motional equivalent circuit elements contributed from the pure film were recorded. Sequential exposure of the film-coated TSM resonator to varying concentrations of benzene, chloroform, n-hexane, and dichloromethane vapors (Sigma-Aldrich, HPLC grade) followed using the dilution system discussed in Section 4.1.1. Between each concentration, the vapor was allowed to fully desorb from the film by purging the test cell with pure nitrogen gas. The motional equivalent circuit elements and resonant frequency of the film-coated resonator upon vapor sorption were recorded continuously in real-time for each solvent exposure iteration. Including vapor generation and data logging from the impedance analyzer, the entire apparatus was computer controlled through Labview 7.0.

4.2 Radial Mass Sensitivity Distribution Measurements of TSM Resonators

Section 4.2 provides details of the experimental technique to measure the mass sensitivity distributions of modified electrode TSM resonators including the process of fabricating the TSM resonators, a detailed schematic of the experimental apparatus, and procedure.

4.2.1 Modified Electrode TSM Resonator Fabrication

To produce the modified electrode TSM resonators, a simple photolithographic process and metal deposition were conducted. The blank quartz substrates utilized were polished 1-inch diameter AT-cut crystals with an operating frequency of 5 MHz (Tangidyne Corp.). These quartz blanks were cut by the manufacturer at an angle of 35º with a one-minute precision and polished with 0.01 μm grit. A 2.0 ml droplet of photoresist (Futurrex, Inc., NR9-1500PY) was deposited at the center of the blank and spun-off at 3500 rpm for 30 seconds in a spin-coater (Laurell Tech.). The resulting thickness of the resist layer was not characterized. Once the photoresist was soft-baked in an oven at 90°C for 15 minutes, it was exposed to viable electrode designs on a high-resolution chromium/glass photomask (Advanced Reproductions Corp.) using a long-wave (365 nm) UV lamp for 45 seconds (Blak-Ray, model B-100W). After exposure, the resist-coated crystal was baked again in the oven at 120°C for another 15 minutes, and developed in developer solution followed by a rinsing in deionized water. The chromium adhesion and gold layers were deposited slowly at a rate of 0.1 Å/s under ultra-high vacuum (~10^{-6} torr) to the desired thicknesses in a thermal evaporator, approximately 75 ± 10 Å and 1050 ± 10 Å, respectively. Lift-off of the photoresist was done in acetone and facilitated in a sonic water bath. The fabrication process was repeated for both sides of the crystal. Good adhesion of the metallic electrode layers to the quartz surface was observed.

4.2.2 Experimental Techniques for Radial Mass Sensitivity Measurements

Various techniques to measure the mass sensitivity across the surface plane of a TSM resonator have been developed including x-ray diffraction to characterize the quartz particle vibration, surface charge distribution measurement, and characterization of optical speckle patterning produced by coherent light incident across the quartz surface. However, all of these methods have significant limitations including the expense of equipment and processing time. Further details are available in Refs. [2], [1], and [40].

4.2.3 Experimental Apparatus

A schematic of the experimental apparatus for measuring the mass sensitivity profile of any TSM resonator is given in Figure 4.2. A discussion of the function of each component is incorporated in the experimental procedure given in Section 4.2.4.

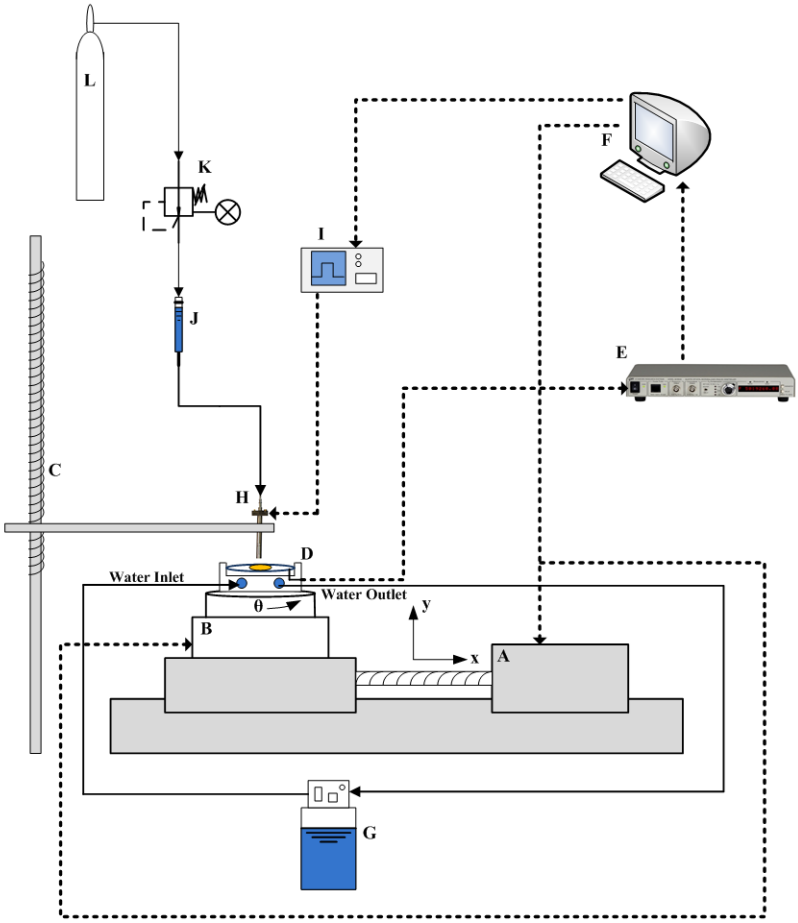

A – Newmark Systems Linear Micropositioner
B – Newmark Systems Rotary Micropositioner
C – Manual Vertical Micropositioner
D – TSM Resonator Stainless-Steel Test Cell
E – Stanford Research Systems QCM200 Frequency Counter and Oscillator Circuit
F – Computer Workstation
G – Thermo Neslab RTE 740 Heater/Chiller Water Circulator
H – TechElan Microvalve with Driver
I – Agilent Pulse Generator
J – Gas Driven Syringe
K – Marsh Bellofram Low Pressure Regulator
L – Nitrogen Cylinder

Figure 4.2: Experimental apparatus for mass sensitivity measurements of TSM resonators.

4.2.4 Experimental Procedure

An approach for measuring the mass sensitivity distribution of a TSM resonator is an ink dot method where dots from a fine-tipped felt pen are placed at precise radial positions and the resulting frequency shifts are recorded. This technique is effective and

efficient provided that the mass of each dot deposited is reproducible. In this study, a novel apparatus was developed using a similar technique; however, the issue of reproducible mass upon each deposit is eliminated. The modified TSM resonators were placed in a stainless steel test cell with drilled channels allowing heated water circulation for maintaining temperature, set at 60°C, and facilitating droplet evaporation. The frequency of the bare crystal at the system temperature was monitored using a high-precision frequency counter (± 0.01 Hz) and simple oscillating circuit (SRS, model QCM-200), and allowed to stabilize. Mass sensitivity measurements were made by depositing minute droplets of a 0.65 wt % hydroxypropylcellulose (HPC)/water solution using a microvalve (TechElan, model SMLD-5b, < 5% CV in dispensing) at radial positions extending from the resonator center. Droplet mass was measured by dispensing 150 droplets into a weighing dish filled with oil and measuring the resultant mass with a mechanical balance. The precise positioning of the droplets along a radial axis was achieved using both a Newmark Systems linear (model NLE-50, 0.01 μm resolution) and rotary (model RT-2, 0.32 arc-seconds resolution) micro-positioner. After deposition of a droplet, the frequency of the resonator was allowed to stabilize to ensure complete evaporation and the resulting shift determined. Based on the known mass deposited and the frequency shift, the mass sensitivity at a radial position is quantified. Measurements were taken along radial axes extending from $\theta = 0°$ to 180° with a step-interval of 30° to account for any anisotropic effects due to the quartz substrate. Experimental details are given in Table 3.1.

Table 3.1: Experimental details for mass sensitivity measurements of the modified TSM resonators

Parameter	Value
Droplets per position	2
HPC mass deposited per position, ng	227 ± 20
Position step interval, mm	0.5

4.3 Droplet Gravimetric Measurements of NVR in Solvents

Section 4.3 describes the experimental process for determining the level of NVR in solvents by droplet gravimetry using the modified TSM resonators.

4.3.1 Experimental Procedure

In this study, incorporation of the fabricated modified TSM resonators into the Masscal^{TM} G1 quartz crystal microbalance/heat conduction calorimeter was attempted to measure the NVR in solvent solutions by droplet gravimetry (www.masscal.com). The G1 consists of a thermopile/aluminum heat sink and a simple oscillator circuit with frequency counter for simultaneous measurement of thermal power and resonator frequency shift. Monitoring of heat flow and frequency shift allows for determining droplet volume (utilizing the latent heat of vaporization) and NVR residue mass accumulation on the TSM device surface, respectively. Figure 4.3 provides a detailed schematic of the G1 instrument.

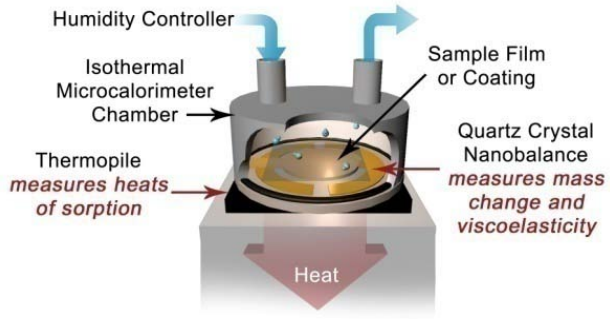

Figure 4.3: Mass/heat flow sensor and sample chamber of the Masscal^{TM} G1.

Droplet gravimetry is conducted in the G1 by depositing microliter size droplets of the solvent using a graduated syringe onto the resonator surface in the sample chamber and monitoring the thermal power flow and frequency shift until the system stabilizes. It is essential that the system stabilize to ensure that the droplet has evaporated to dryness. NVR levels in solvents are determined by droplet gravimetry from the following equations [48].

$$\Delta f = -C_f \frac{m_r}{A_r} \tag{4.1}$$

$$Q = \int P(t)dt = \frac{\rho_s \mathrm{V_s} \Delta H_s^{vap}}{M_s} \tag{4.2}$$

Here, Δf is the frequency shift associated with the residue deposited, m_r and A_r are the residue film mass and area, respectively, and C_f is the sensitivity factor. For a 5 MHz TSM device, the sensitivity factor is taken to be 56.3 Hz*cm^2/μg. Additionally, Q and $P(t)$ are the integral heat required to evaporate the droplet and the measured thermal power, ρ_s and V_s are the solvent density and volume, ΔH_s^{vap} is the latent heat of vaporization of the solvent, and M_s is the molar mass of the solvent.

CHAPTER 5

RESULTS AND DISCUSSION

5.1 Viscoelastic Shear Moduli of Poly(isobutylene)/Solvent Systems

Using the measured motional circuit elements of the TSM resonator, the model in Section 2.5.2 was used to extract the storage, *G'*, and loss, *G"*, moduli for the pure and solvent-loaded poly(isobutylene) films presented in this work. Figures 5.1 through 5.4 present these results. The trends in the shear modulus components for these systems match a similar study characterizing the effect of temperature change on a pure viscoelastic poly(isobutylene) film [9], as well as, a study of vapor sorption in another rubbery polymer, poly(dimethyl siloxane) (PDMS), [50]. This correlation further emphasizes the viability of characterizing the dynamic behavior of an excited bulk film through analyzing its effects on the electrical/mechanical response of a TSM resonator. Error in the result measurements, denoted in the error bars expressing one standard deviation, is attributed to the uncertainty in the initial thickness of the pure poly(isobutylene) film deposited on the surface of the resonator which was measured by profilometry to be approximately 13.0 ± 0.2 μm. It should be noted the viscoelastic shear moduli is a physical film property that should be independent of film thickness, however, the impedance model derived in Section 2.5.2 is sensitively dependent on film properties. Meaning for a given motional response of a TSM resonator to a coupled mass loading, accurate pure or mixture film properties are necessary.

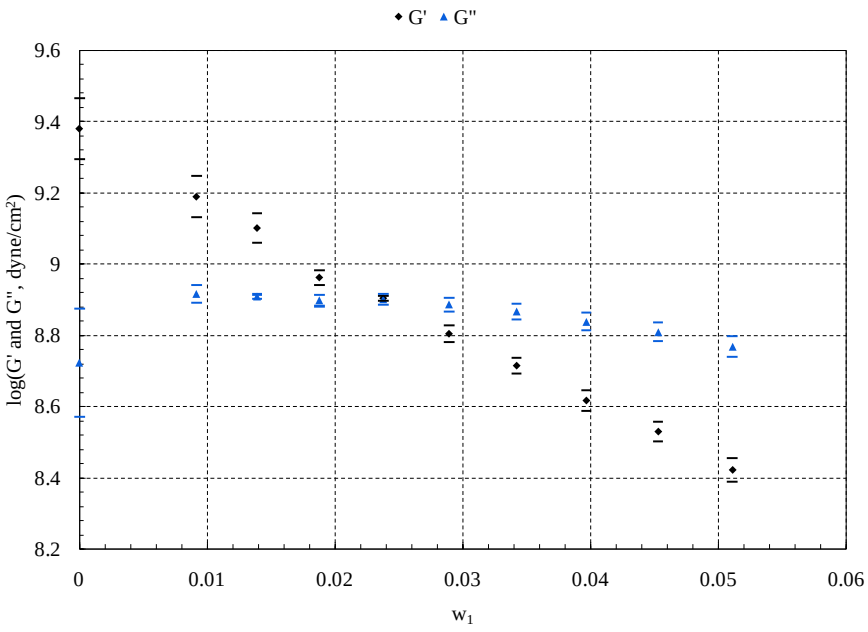

Figure 5.1: Measured storage, *G'*, and loss, *G"*, moduli of poly(isobutylene)/benzene systems versus benzene weight fraction, w_1.

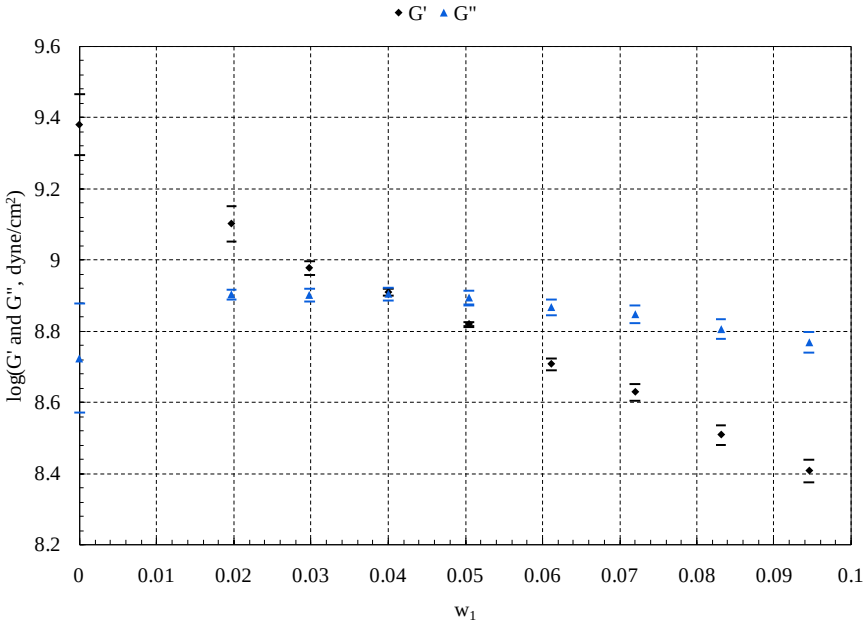

Figure 5.2: Measured storage, *G'*, and loss, *G"*, moduli of poly(isobutylene)/chloroform systems versus chloroform weight fraction, w_1.

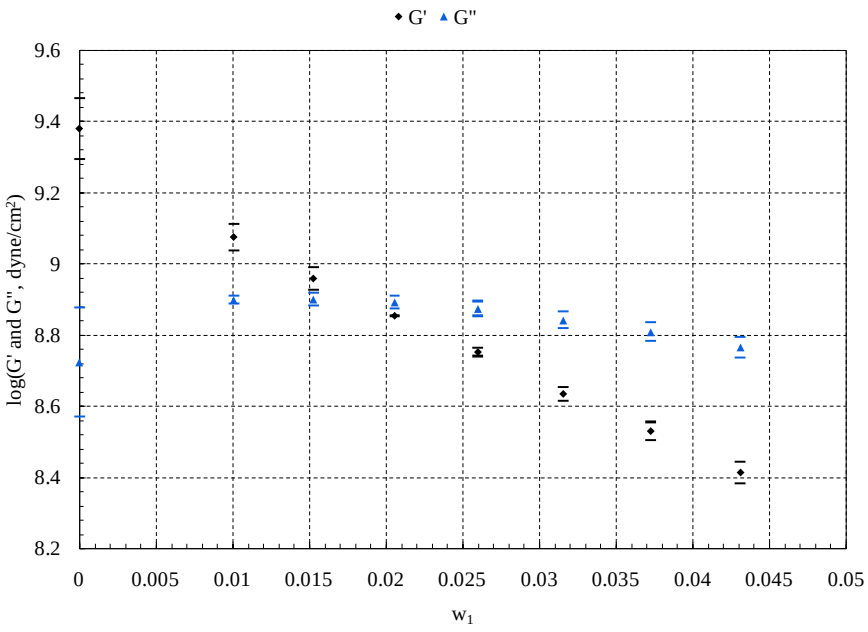

Figure 5.3: Measured storage, *G'*, and loss, *G"*, moduli of poly(isobutylene)/n-hexane systems versus n-hexane weight fraction, w_1.

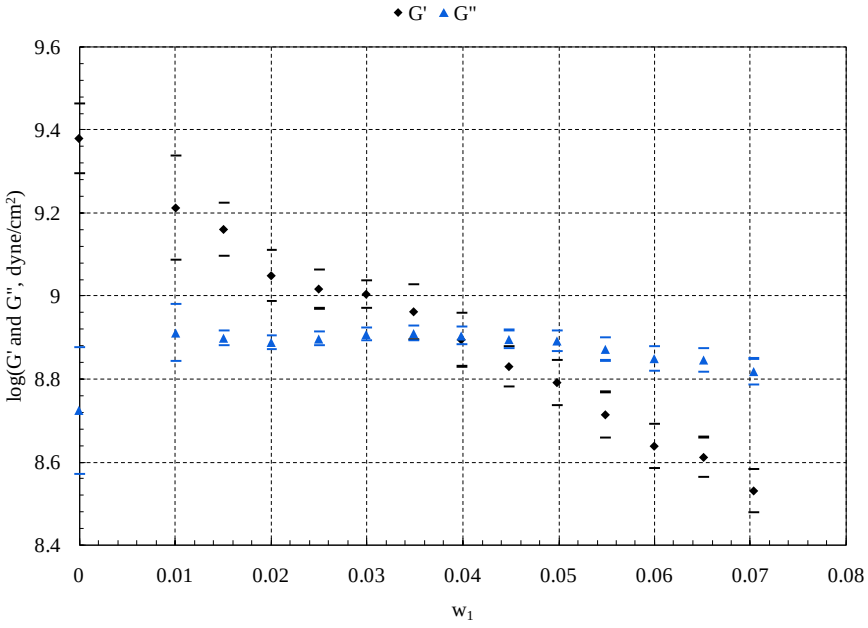

Figure 5.4: Measured storage, *G'*, and loss, *G"*, moduli of poly(isobutylene)/ dichloromethane systems versus dichloromethane weight fraction, w_1.

5.2 Fractional Free-Hole Volume of Poly(isobutylene)/Solvent Systems

Results for the experimental fractional free-hole volume for the poly(isobutylene)/solvent systems compared to the Vrentas-Duda FV theory are presented in Figures 5.5 through 5.8. The experimental results were determined using the measured shear modulus components presented in Section 5.1 and the superposition principle in Section 2.6.1. A linear trend in the fractional free-hole volume data with solvent weight fraction is observed which is expected given the high correlation with the FV model. Deviation in the experimental data from the empirical model can be attributed to the choice in the value of the fractional free-hole volume for a pure poly(isobutylene) film, either measured directly using a TSM resonator or obtained from literature. Additionally, the free volume parameters employed in the Vrentas-Duda FV theory can vary depending on the accuracy of the temperature-pressure viscosity data from which they are determined.

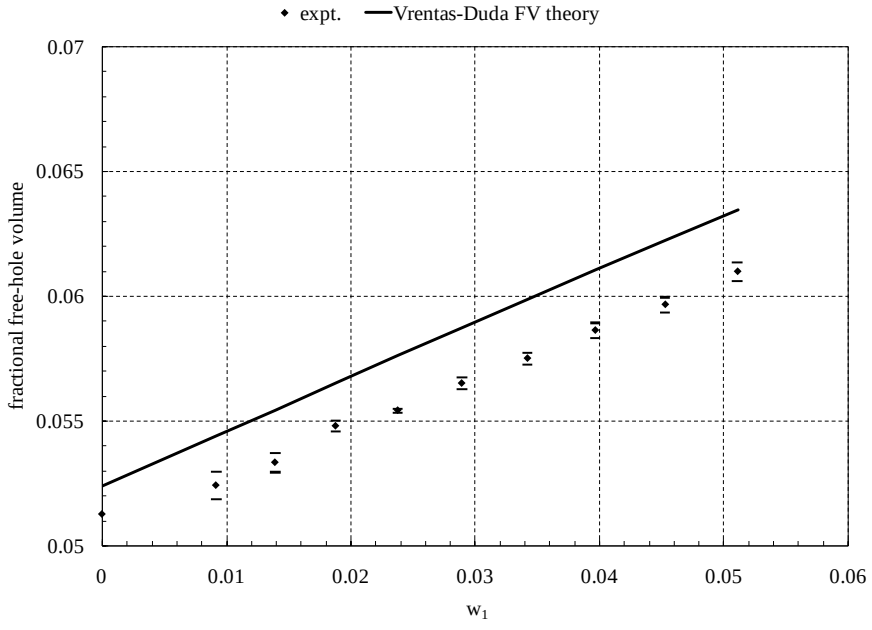

Figure 5.5: Experimental fractional-free hole volume of poly(isobutylene)/ benzene systems compared to the Vrentas-Duda FV model.

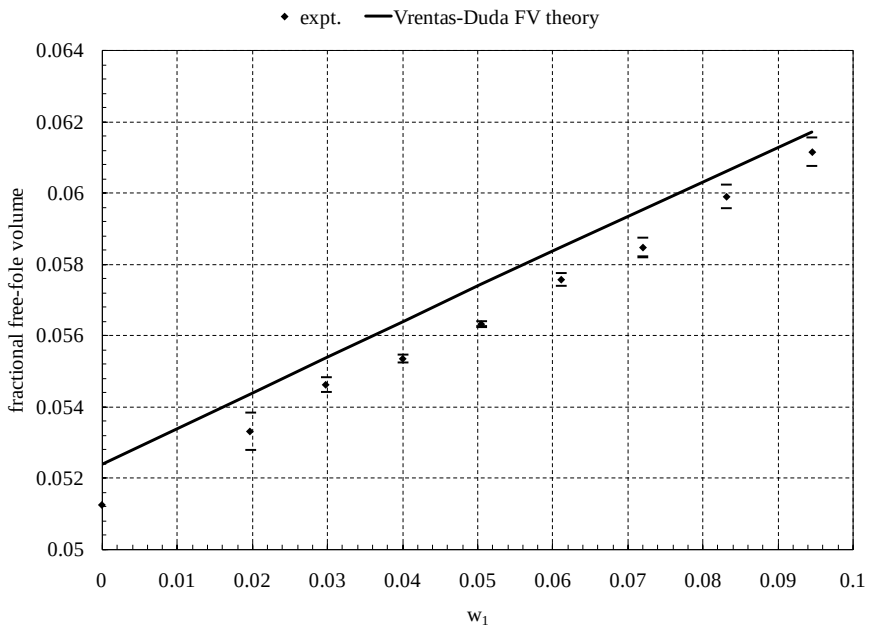

Figure 5.6: Experimental fractional-free hole volume of poly(isobutylene)/ chloroform systems compared to the Vrentas-Duda FV model.

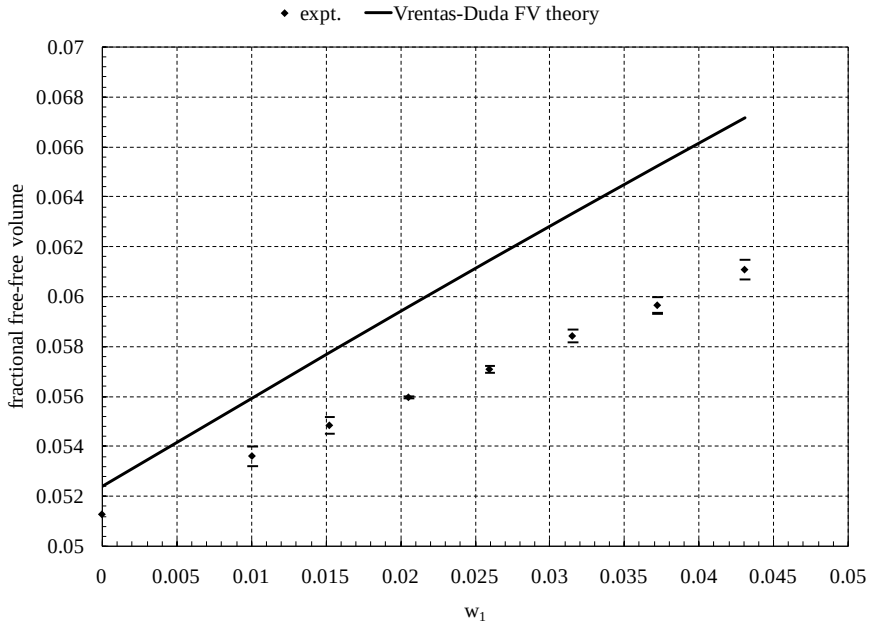

Figure 5.7 Experimental fractional-free hole volume of poly(isobutylene)/n-hexane systems compared to the Vrentas-Duda FV model.

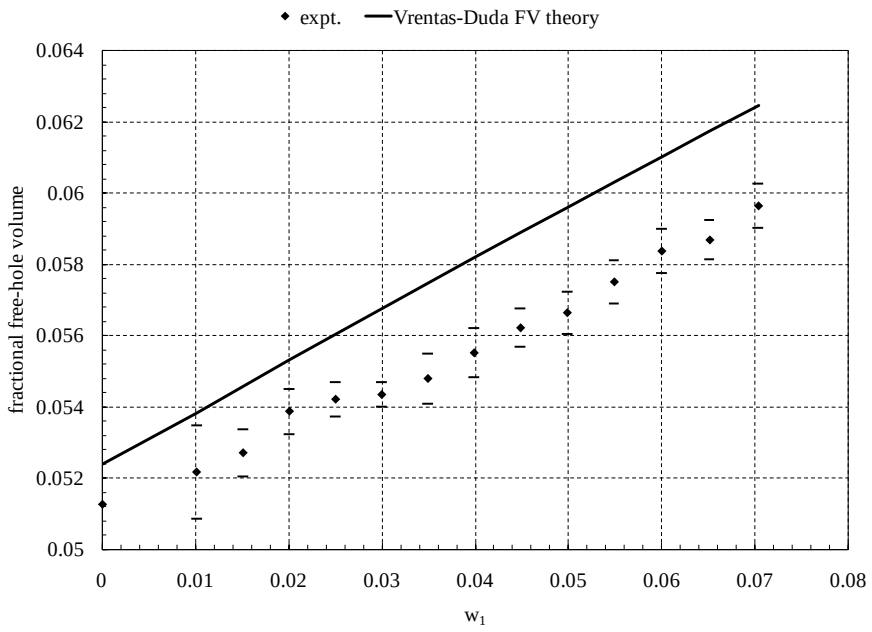

Figure 5.8: Experimental fractional-free hole volume of poly(isobutylene)/ dichloromethane systems compared to the Vrentas-Duda FV model.

5.3 Mass Sensitivity Measurements of Electrode Modified TSM Resonators

Using the model predicted R value and 4-10 mm ring electrode configuration discussed in Section 3.4, devices were fabricated and tested. Figure 5.9 presents the experimental mass sensitivity measurements. The experimental results represent multiple measurements taken over different radial alignments extending from $\theta = 0°$ to 180° with a step-interval of 30°. Results agree well with theory, however, there still exists a remnant bimodal response in the distribution. Uncertainty in the electrode thicknesses, approximately ±10 Å, explains the discrepancy given that the mass sensitivity profile is sensitively dependent on the electrode mass loading. Additionally, variable scatter in the measured data, denoted in the error bars expressing one standard deviation, was observed. Anisotropy of the quartz is likely a contributor to the approximately 10-15% standard deviation (error bars) reported in Figure 5.9, where data are averaged over all radial directions. This situation improves when mass sensitivity is measured along a single radial direction, in which case the standard deviation is 3%. However, it is

difficult to design a practical nanobalance wherein mass is deposited along a single radial direction. Hence, data averaged over all radial directions have been presented. The inherent vibration instability of the ring electrode configuration due to energy trapping resulting from the coupling of the oscillating modes within the electroded region, between the radii *a* and *b*, [38, 39] also contributes to the scatter.

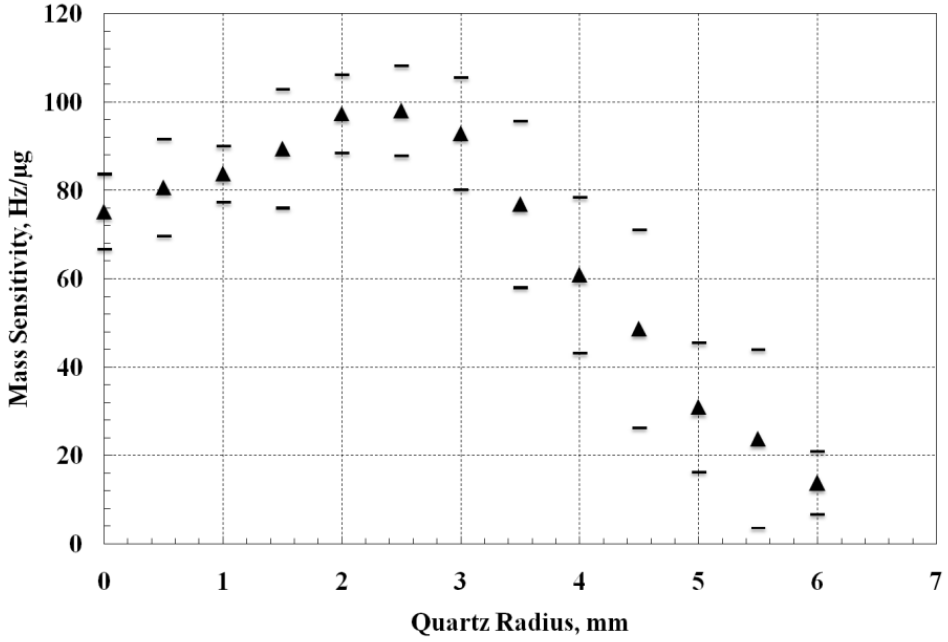

Figure 5.9: Experimental mass sensitivity distribution for a ring electrode 5 MHz TSM device having inner and outer diameters of 4 and 10 mm, respectively, with R = 0.0025.

5.4 Droplet Gravimetry Measurements Using Electrode Modified TSM Resonators

Initial NVR measurements in histological grade methanol (Fisher Scientific) were conducted using the G1 microbalance/calorimeter and the modified TSM resonators. The results from these measurements exhibited unreasonable standard deviations in the NVR. The microliter sized droplets dispensed from the syringe are too large for the modified TSM devices due to wetting effects prompting spreading of the droplets outside the sensing area of the device. Incorporation of a microvalve into the G1 would eliminate this

shortcoming and allow accurate measurement of NVR by droplet gravimetry. Additionally, chemical modification of the gold surface with an alkanethiol self-assembled monolayer (SAM) would create a hydrophobic/hydrophilic surface for droplet containment.

An equivalent method for determining NVR in solvent droplets using the mass sensitivity apparatus was utilized (see Figure 4.2). Droplets of methanol were deposited using the microvalve within the area of constant mass sensitivity of the modified TSM resonators and the resulting frequency shifts recorded. The mass of each droplet was determined to be 170.1 ± 8.4 μg by dispensing 150 droplets in a weighing tray full of oil and weighed using a mechanical mass balance (Denver Instrument Company, model 250-A, 0.01 mg tolerance). The 5% discrepancy in the droplet mass can be attributed to both the potential evaporation of methanol before it reaches the oil and the tolerance of the balance. Droplet mass can also be determined from the integral heat associated with the droplet evaporation on the TSM device surface; with the incorporation of a microvalve for nanoliter dispensing in the Masscal G1 nanobalance/calorimeter. Given a residue film area of approximately 0.042 cm^2, determined by optical measurement of the residue radius, the residue mass and resulting NVR levels were calculated. The optical measurements of the film radius were made using a transmission microscope (Leica, model DMI-4000B, 5 μm resolution). Detailed droplet gravimetric results are given in Table 4.1.

Table 4.1: Detailed droplet gravimetric results

Droplet #	Δf, (Hz)	m_r, (ng)	NVR, (ppm)
1	-1.26	0.94	5.49
2	-1.55	1.16	6.77
3	-0.98	0.73	4.28
4	-1.12	0.83	4.88
5	-1.62	1.21	7.09
total	-6.53	4.84	5.70±1.2*

* denotes average and standard deviation

The gravimetric results of NVR levels in the methanol droplets are encouraging, given that they are within the range expected for the histological grade methanol utilized, even though the standard deviation in NVR is relatively high. NVR measurements of stock methanol solutions having a volume of 150 ml were conducted for comparison. These solutions were completely evaporated at 100°C in a water bath and dried in a vacuum oven for one hour at 101°C. The residues were carefully weighed and, based on a methanol density of 0.7918 g/ml disclosed by the solvent manufacturer, the stock NVR level was determined to be within the range of 4.2 to 5.0 ppm. Although there is good agreement between the droplet gravimetric and bulk volume evaporation NVR results, further improvement of the modified TSM devices is necessary to reduce the standard deviation observed.

CHAPTER 6

CONCLUSIONS AND FUTURE WORK

In summary, two applications of TSM resonators were studied in this thesis work. Firstly, a technique was proposed to determine the fractional free-hole volume of poly(isobutylene)/solvent systems from viscoelastic shear moduli, G, data of these systems measured using a TSM resonator. Reasonable agreement between experimental results and empirical modeling indicates the technique is viable and can be used to evaluate the fractional free-hole volume for any polymer/solvent system which is necessary to evaluate diffusion dynamics. However, extension to other systems requires the study of the viscoelastic behavior of other pure films to generate "master curves."

Secondly, a ring electrode design (with appropriate electrode mass loading factor) that produces a uniform mass sensitivity distribution across a TSM device is presented in this study. A new technique and apparatus to measure this mass sensitivity distribution is also presented. Fabricated devices utilizing model predictions were tested using this apparatus, and good agreement between theory and experiment is found. A viable TSM device that can be utilized to construct a nanobalance is the result of this work, however, improvements are possible, both in terms of improved stability of the device resonance frequency and more uniform sensitivity distribution over a larger device surface. Such designs require extensions of the analytical model utilized in this work, or finite element simulations, to geometries other than the ring electrode design.

REFERENCES

[1] P. J. Cumpson, "Quartz crystal microbalance: A new design eliminates sensitivity outside the electrodes, often wrongly attributed to the electric fringing field," *J. Vac. Sci. Tech. A*, vol. 15, pp. 2407-2412, 1997.

[2] P. J. Cumpson, and M. P. Seah, "The quartz crystal microbalance; radial/polar dependence of mass sensitivity both on and off the electrodes," *Meas. Sci. Tech.*, vol. 1, pp. 544-555, 1990.

[3] J. D. Ferry, *Viscoelastic Properties of Polymers*, 3rd ed., Hoboken, NJ: John Wiley & Sons, 1980.

[4] B. Morray, S. Li, J. Hossenlopp *et al.*, "PMMA polymer film characterization using thickness-shear mode (TSM) quartz resonator," *IEEE Intern. Freq. Contr. Symp., New Orleans, LA*, pp. 294-300, 2002.

[5] M. H. Cohen, and D. J. Turnbull, "Molecular transport in liquids and glasses," *J. Chem. Phys.*, vol. 31, pp. 1164-1169, 1959.

[6] S. Hong, J. L. Duda, and D. C. Venerus, "Diffusion of organic solvents in isobutylene-based polymers," *Korean J. of Chem. Eng.*, vol. 13, pp. 255-260, 1996.

[7] A. Thran, G. Kroll, and F. Faupel, "Correlation between fractional free volume and diffusivity of gas molecules in glassy polymers," *J. Polym. Sci. B: Polym. Phys.*, vol. 37, pp. 3344-3358, 1999.

[8] D. Kilburn, J. Wawryszczuk, G. Dlubek *et al.*, "Temperature and pressure dependence of the free volume in polyisobutylene from positron lifetime and pressure-volume-temperature experiments," *Macromol. Chem. Phys.*, vol. 207, pp. 721-734, 2006.

[9] S. J. Martin, and G. C. Frye, "Polymer film characterization using quartz resonators," *IEEE Ultrasonics Symp.*, pp. 393-398, 1991.

[10] A. K. Upadhyayula, "Sorption of Organic Vapors by Copolymers of Poly(Styrene-Butadiene) Using a Piezoelectric Microbalance," Master's Thesis, Chemical Engineering, University of South Florida, Tampa, FL, 2005.

[11] C. Tsonopoulos, "An empirical correlation of second virial coefficients," *AIChE J.*, vol. 20, pp. 263-272, 1974.

[12] J. M. Smith, H. C. V. Ness, and M. M. Abbott, *Introduction to Chemical Engineering Thermodynamics*, 7th ed., New York, NY: McGraw Hill, 2005.

[13] R. C. Reid, J. M. Prausnitz, and T. K. Sherwood, *The Properties of Gases and Liquids*, 3rd ed., New York, NY: McGraw Hill, 1978.

[14] P. J. Flory, "Thermodynamics of high polymer solutions," *J. Chem. Phys.*, vol. 9, pp. 660, 1941.

[15] M. L. Huggins, "Solutions of long chain compounds," *J. Chem. Phys.*, vol. 9, pp. 440, 1941.

[16] J. M. Prausnitz, R. N. Lichtenthaler, and E. G. d. Azevedo, "Molecular Thermodynamics of Fluid-Phase Equilibria," Upper Saddle River, NJ: Prentice Hall, 1999.

[17] A. Fredenslund, A. J. Gmechling, and P. Rasmussen, *Vapor-Liquid Equilibria Using UNIFAC*, Amsterdam, The Netherlands: Elsevier, 1977.

[18] T. Oishi, and J. M. Prausnitz, "Estimation of solvent activities in polymer solutions using a group-contribution method," *Ind. Eng. Chem. Proc. Des. Dev.*, vol. 17, no. 3, pp. 333, 1978.

[19] G. M. Kontogeorgis, and A. Fredenslund, "Simple activity coefficient model for the prediction of solvent activities in polymer solutions," *Ind. Eng. Chem. Res.*, vol. 32, pp. 362-372, 1993.

[20] S. J. Martin, V. E. Granstaff, and G. C. Frye, "Characterization of a quartz crystal microbalance with simultaneous mass and liquid loading," *Analytical Chem.*, vol. 63, pp. 2272-2281, 1991.

[21] G. Sauerbrey, "The use of quartz oscillators for weighing thin films and for microweighing," *Z. Phys.*, vol. 155, pp. 206-222, 1959.

[22] B. S. Ballantine, R. M. White, S. J. Martin *et al.*, *Acoustic Wave Sensors: Theory, Design, and Physico-Chemical Applications*, Boston, MA: Academic Press, Inc., 1997.

[23] R. Williams, "Organic Vapor Sensing Using High Frequency Thickness Shear Mode Resonators," Master's Thesis, Chemical Engineering, University of South Florida, Tampa, FL, 2005.

[24] S. J. Martin, and G. C. Frye, "Dynamics and response of polymer-coated surface acoustic wave devices: effect of viscoelastic properties and film resonance," *Analytical Chem.*, vol. 66, pp. 2201-2219, 1994.

[25] A. Ballato, "Frequency-temperature-load capacitance behavior of resonators for TCXO application," *IEEE Trans. Sonics Ultrason.*, vol. SU-25, no. 4, pp. 185-191, 1978.

[26] J. Hossenlopp, L. Jiang, R. Cernosek *et al.*, "Characterization of epoxy resin (SU-8) film using thickness-shear mode (TSM) resonator under various conditions " *J. Polym. Sci. B: Polym. Phys.*, vol. 42, pp. 2373-2384, 2004.

[27] J. F. Rosenbaum, *Bulk Acoustic Wave Theory and Devices*, Boston, MA: Artech, 1988.

[28] H. L. Bandey, S. J. Martin, R. W. Cernosek *et al.*, "Modeling the responses of thickness-shear mode resonator with a viscoelastic film near film resonance," *Analytical Chem.*, vol. 72, pp. 141-149, 2000.

[29] O. Wolff, E. Seydel, and D. Johannsmann, "Viscoelastic properties of thin films studied with quartz resonators," *Faraday Discuss.*, vol. 107, pp. 91-104, 1997.

[30] J. J. Aklonis, and W. J. MacKnight, *Introduction to Polymer Viscoelasticity*, New York, NY: John Wiley and Sons, 1983.

[31] M. L. Williams, R. F. Landel, and J. D. Ferry, "The temperature dependence of relaxation mechanisms in amorphous polymers and other glass-forming liquids," *J. Am. Chem. Soc.*, vol. 77, pp. 3701-3707, 1955.

[32] A. K. Doolittle, and D. B. Doolittle, "Studies in Newtonian flow. V: further verification of the free-space viscosity equation," *J. Appl. Phys.*, vol. 28, pp. 901-905, 1957.

[33] B. Wang, H. Lv, and J. Yang, "Estimation of solvent diffusion coefficient in amorphous polymers using the Sanchez-Lacombe equation-of-state," *Chem. Eng. Sci.*, vol. 62, pp. 775-782, 2007.

[34] R. Simha, and T. Somcynsky, "On the statistical thermodynamics of spherical and chain molecule fluids," *Macromolecules*, vol. 2, pp. 342-350, 1969.

[35] J. S. Vrentas, and J. L. Duda, "Diffusion in polymer-solvent systems. I: reexamination of the free-volume theory," *J. Polym. Sci. B: Polym. Phys.*, vol. 15, pp. 403-416, 1977.

[36] J. S. Vrentas, and J. L. Duda, "Diffusion in polymer-solvent systems. II: a predictive theory for the dependence of diffusion coefficients on temperature, concentration, and molecular weight," *J. Polym. Sci. B: Polym. Phys.*, vol. 15, pp. 417-439, 1977.

[37] W. R. Foss, J. N. Anderl, A. L. Clausi *et al.*, "Diffusivities of dichloromethane in poly(lactide-co-glycolide," *J. Appl. Polym. Sci.*, vol. 112, pp. 1622-1629, 2009.

[38] F. Josse, Y. Lee, S. J. Martin *et al.*, "Analysis of the radial dependence of mass sensitivity for modified-electrode quartz resonators," *Analytical Chem.*, vol. 70, pp. 237-247, 1998.

[39] E. Ansorge, K. Pitschmann, B. Schmidt *et al.*, "Plano-convex shaped langasite microbalances for high temperature applications," *IEEE Sensors Conference, Atlanta, GA*, pp. 1424-1427, 2007.

[40] V. M. Mecea, "A new method of measuring the mass sensitive areas of quartz crystal resonators," *J. Phys. E: Sci. Instr.*, vol. 22, pp. 59-61, 1989.

[41] M. D. Ward, and E. J. Delawski, "Radial mass sensitivity of the quartz crystal microbalance in liquid media," *Analytical Chem.*, vol. 63, pp. 886-890, 1991.

[42] Y. Lee, "The Quartz Crystal Resonator: Analysis of the Mechanical and Electrical Loading Sensitivities on Modified-Electrode Surface," Ph.D. Dissertation, Marquette University, Milwaukee, WI, 1996.

[43] F. Lu, H. P. Lee, and S. P. Lim, "Quartz crystal microbalance with rigid mass partially attached on electrode surfaces," *Sens. Actuators A: Phys.*, vol. 112, pp. 203-210, 2004.

[44] Z. Wang, J. David, N. Cheeke *et al.*, "Perturbation method for analyzing mass sensitivity of planar multilayer acoustic sensors," *IEEE Trans. Ultrason., Ferroelect., Freq. Contr.*, vol. 43, pp. 844-851, 1996.

[45] S. W. Wenzel, and R. M. White, "Analytic comparison of the sensitivities of bulk-wave, surface-wave, and flexural plate-wave ultrasonic sensors," *Appl. Phys. Lett.*, vol. 54, pp. 1976-1978, 1989.

[46] H. F. Tiersten, *Linear Piezoelectric Plate Vibrators: Elements of the Linear Theory of Piezoelectricity and the Vibrations of Piezoelectric Plates*, New York, NY: Plenum Press, 1969.

[47] N. W. McLachlan, *Bessel Functions for Engineers*, London, UK: Clarendon Press, 1955.

[48] A. Smith, "Gravimetric analysis of non-volatile residue from an evaporated droplet, using the quartz crystal microbalance/heat conduction calorimeter," *J. ASTM Intl.*, vol. 3, pp. 1-5, 2006.

[49] A. Smith, and H. M. Shirazi, "Principles of quartz crystal microbalance/heat conduction calorimetry: measurement of the sorption enthalpy of hydrogen in palladium," *Thermochim. Actua.*, vol. 432, pp. 202-211, 2005.

[50] R. C. Holt, G. J. Gouws, and J. Z. Zhen, "Measurement of polymer shear modulus using thickness shear acoustic waves," *Curr. Appl. Phys.*, vol. 6, pp. 334-339, 2006.

APPENDICES

Appendix A: Supplementary Equations

A.1 Cutoff Frequencies from Equation 3.3

The cutoff frequencies, f_c, for each electroded region in Equation 3.3 are [38]:

$$f_c = \begin{cases} \frac{1}{h_q}\sqrt{\frac{\hat{C}_{66}^{P}}{\rho_q}} & 0 \le r \le a \\ \frac{1}{h_q}\sqrt{\frac{\hat{C}_{66}^{E}}{\rho_q}} & a \le r \le b \\ \frac{1}{h_q}\sqrt{\frac{\bar{C}_{66}}{\rho_q}} & b \le r < \infty \end{cases} \tag{A.1}$$

$$f_{66} = \frac{1}{h_q}\sqrt{\frac{C_{66}}{\rho_q}} \tag{A.2}$$

Where,

$$\bar{C}_{66} = C_{66} + \frac{{e_{26}}^2}{\epsilon_{22}} \tag{A.3}$$

$$\hat{C}_{66}^{E} = \bar{C}_{66}\left(1 - 2R - \left(\frac{8{k_{26}}^2}{\pi^2}\right)\right) \tag{A.4}$$

$$\hat{C}_{66}^{P} = \bar{C}_{66}\left(1 - R - \left(\frac{8{k_{26}}^2}{\pi^2}\right)\right) \tag{A.5}$$

$${k_{26}}^2 = \frac{{e_{26}}^2}{\bar{C}_{66}\epsilon_{22}} \tag{A.6}$$

Here, C_{66}, e_{26}, and ϵ_{22} are the elastic stiffness, piezoelectric, and dielectric constants of AT-cut quartz. R is the electrode mass loading factor.

Appendix A: (continued)

A.2 Definite Integral in Equation 3.1

The definite integral in Equation 3.1 is [42]:

$$\begin{aligned}\int_0^\infty r|u_1(r)|^2 dr \\ &= \int_0^a rA^2 {I_0}^2\left(k_r^p r\right)dr \\ &+ \int_a^b r\left[B^2 {J_0}^2(k_r^e r) + C^2 {N_0}^2(k_r^e r)\right. \\ &\left. + 2BCJ_0(k_r^e r)N_0(k_r^e r)\right]dr + \int_b^\infty rD^2 {K_0}^2(k_r^u r)dr\end{aligned} \tag{A.7}$$

Where,

$$\int_0^a rA^2 {I_0}^2\left(k_r^p r\right)dr = \frac{A^2}{2}a^2\left[{I_0}^2\left(k_r^p a\right) - {I_1}^2\left(k_r^p a\right)\right] \tag{A.8}$$

Appendix A: (continued)

$$\int_a^b r\left[B^2 {J_0}^2(k_r^e r) + C^2 {N_0}^2(k_r^e r) + 2BCJ_0(k_r^e r)N_0(k_r^e r)\right]dr$$
$$= \frac{B^2}{2} b^2\left[{J_0}^2(k_r^e b) + {J_1}^2(k_r^e b)\right] -$$
$$\frac{A^2}{2} a^2\left[{J_0}^2(k_r^e a) + {J_1}^2(k_r^e a)\right] +$$
$$\frac{C^2}{2} b^2\left[{N_0}^2(k_r^e b) + {N_1}^2(k_r^e b)\right] - \quad \text{(A.9)}$$
$$\frac{C^2}{2} a^2\left[{N_0}^2(k_r^e a) + {N_1}^2(k_r^e a)\right] +$$
$$BCb^2[J_0(k_r^e b)N_0(k_r^e b) + J_1(k_r^e b)N_1(k_r^e b)] -$$
$$BCa^2[J_0(k_r^e a)N_0(k_r^e a) + J_1(k_r^e a)N_1(k_r^e a)]$$

$$\int_b^\infty rD^2 {K_0}^2(k_r^u r)dr = \frac{D^2}{2} b^2\left[{K_1}^2(k_r^u b) - {K_0}^2(k_r^u b)\right] \quad \text{(A.10)}$$